## Bayesian analysis of capture reactions ${}^{3}\text{He}(\alpha,\gamma){}^{7}\text{Be}$ and ${}^{3}\text{H}(\alpha,\gamma){}^{7}\text{Li}$

Pradeepa Premarathna\* and Gautam Rupak<sup>†</sup> Department of Physics & Astronomy and  $HPC^2$  Center for Computational Sciences, Mississippi State University, Mississippi State, MS 39762, USA

Bayesian analysis of the radiative capture reactions  ${}^3\text{He}(\alpha,\gamma){}^7\text{Be}$  and  ${}^3\text{H}(\alpha,\gamma){}^7\text{Li}$  are performed to draw inferences about the cross sections at threshold. We do a model comparison of two competing effective field theory power countings for the capture reactions. The two power countings differ in the contribution of two-body electromagnetic currents. In one power counting, two-body currents contribute at leading order, and in the other they contribute at higher orders. The former is favored for  ${}^3\text{He}(\alpha,\gamma){}^7\text{Be}$  if elastic scattering data in the incoming channel is considered in the analysis. Without constraints from elastic scattering data, both the power countings are equally favored. For  ${}^3\text{H}(\alpha,\gamma){}^7\text{Li}$ , the first power counting with two-body current contributions at leading order is favored with or without constraints from elastic scattering data.

Keywords: Bayesian inference, radiative capture, halo effective field theory

## I. INTRODUCTION

Effective field theory (EFT) calculations of low-energy capture reactions provide important uncertainty estimates in cross section evaluations. Element synthesis in the Big Bang and in stellar environments involve reactions at low energies. These reaction rates are suppressed by the Coulomb repulsion at low energy, making their measurements challenging. For example, the proton-proton fusion rate is not known experimentally at the relevant solar energy [1]. Theory is needed to extrapolate measurements at higher energies to the astrophysically relevant lower energies. EFT extrapolations are attractive as they provide model-independent error estimates. The basic idea in the EFT formulation is that one only considers certain degrees of freedom as dynamical at low momentum p below a cutoff  $\Lambda \gg p$ . The physics associated with the high-momentum scale  $\Lambda$  is not modeled but contributes through dimensionful couplings in the low-momentum theory. Observables are calculated as an expansion in  $Q/\Lambda \ll 1$  called the power counting.  $Q \sim p$  characterizes the low-momentum physical scale. Theoretical uncertainties are estimated from powers of  $Q/\Lambda$  at a given order of the perturbative expansion.

Typical radiative capture reactions such as  ${}^3{\rm He}(\alpha,\gamma){}^7{\rm Be}$  and  ${}^3{\rm H}(\alpha,\gamma){}^7{\rm Li}$  considered in this work depend on initial state interaction, electro-weak currents and the final state wave function. Information about the initial state interaction at low momentum can be incorporated by matching the EFT couplings to elastic scattering phase shifts. The final state physics is contained in the bound state energy and the asymptotic wave function normalization which can be determined from the relevant phase shift as well. The one-body electro-weak currents are well determined, and usually they give the dominant contribution. A difficulty in these calculations is that the low momentum phase shifts

are poorly known which introduces large uncertainty in the construction of the EFT interactions. Moreover, in systems that involve weakly-bound states the couplings can be fine tuned such that two-body currents contribute at leading order (LO) of the perturbation [2].

The low-energy capture reactions  ${}^{3}\text{He}(\alpha,\gamma){}^{7}\text{Be}$  and  ${}^{3}\text{H}(\alpha,\gamma){}^{7}\text{Li}$  are of great interest in nuclear astrophysics. The reactions  ${}^{3}\text{He}(\alpha,\gamma){}^{7}\text{Be}(p,\gamma){}^{8}\text{B}$  provide the high energy  ${}^{8}\text{B}$  neutrinos detected at Super-K [3] and SNO [4]. The neutrino flux is proportional to the  ${}^{3}\text{He}(\alpha,\gamma){}^{7}\text{Be}$  cross section  $\sigma$  near its Gamow energy  $E_{G} \sim 20$  keV as  $\sigma^{0.81}$  [5, 6]. Several measurements of the  ${}^{3}\text{He}(\alpha,\gamma){}^{7}\text{Be}$  capture rate have been performed in recent decades, for example [7–11]. The reaction  ${}^{3}\text{H}(\alpha,\gamma){}^{7}\text{Li}$  is important for calculating  ${}^{7}\text{Li}$  abundances, constraining astrophysical models of Big Bang Nucleosynthesis [12, 13]. There are less constraints on this reaction from recent measurements [14, 15].

In this work we use Bayesian analysis to revisit the calculation of  ${}^3{\rm He}(\alpha,\gamma){}^7{\rm Be}$  [2], and also extend the analysis to the related reaction  ${}^3{\rm H}(\alpha,\gamma){}^7{\rm Li}$ . Bayesian analysis is useful in situations as these where we have a large number of parameters that are poorly constrained by lack of accurate data especially in the elastic channels. Parameter estimation is important in not only extrapolation of reaction rates to solar energies but also to develop a systematic power counting expansion in  $Q/\Lambda$ . This is crucial for providing theoretical error estimates. Further, Bayesian analysis allows for a quantitative comparison of EFT formulations where, for example, the two-body currents appear at different orders in the perturbation.

The expressions for the cross sections are from Ref. [2] that used halo EFT in the calculations. In halo EFT [16, 17], nuclear clusters are treated as point like particles at momenta that are too small to cause the clusters to break apart. Capture reaction calculations are outlined in the review article Ref. [18]. We consider two power countings depending on the size of the scattering length  $a_0$  in the incoming s-wave channel. In one power counting, two-body currents contribute at LO and in the other they contribute at next-to-leading order (NLO).

<sup>\*</sup> psp63@msstate.edu

<sup>†</sup> grupak@ccs.msstate.edu

## II. HALO EFT CALCULATION

The calculations for  ${}^{3}\text{He}(\alpha,\gamma){}^{7}\text{Be}$  and  ${}^{3}\text{H}(\alpha,\gamma){}^{7}\text{Li}$  are similar. The discussion here follows Ref. [2]. The ground state of <sup>7</sup>Be has a binding energy  $B_0^{\text{(Be)}} = 1.5866 \text{ MeV}$ and spin-parity assignment  $\frac{3}{2}^-$ . The first excited state has a binding energy  $B_1^{\mathrm{(Be)}} = 1.1575 \mathrm{\ MeV}$  and spinparity assignment  $\frac{1}{2}$ . These binding energies are identified with the low-energy scale [2] and they are treated as a bound state of  ${}^{3}\text{He}$  and  $\alpha$  clusters in the calculation. The higher excited states of <sup>7</sup>Be with the same spin-parity as the first two states lie at least about 8 MeV above the  ${}^{3}\text{He-}\alpha$  threshold. These are not included in the low-energy theory. The proton separation energy of <sup>3</sup>He ( $\sim 5.5$  MeV), excited states of  $\alpha (\gtrsim 20$  MeV) are identified with the high-energy scale as well. Thus, we treat the <sup>3</sup>He and  $\alpha$  clusters as point-like fundamental particles. The spin-parity assignments of  $\frac{1}{2}^+$  for the  $^3\mathrm{He}$ and  $0^+$  for the  $\alpha$  implies that the  $\frac{3}{2}^-$ ,  $\frac{1}{2}^-$  states of <sup>7</sup>Be are p-wave bound states of  ${}^{3}\text{He}$  and  $\alpha$ . Then radiative capture at low energy is dominated by E1 transition from s-wave initial states with a small contribution from the d waves [2]. For the  ${}^{3}\mathrm{H}(\alpha,\gamma){}^{7}\mathrm{Li}$  reaction, the ground state of <sup>7</sup>Li has a binding energy  $B_0^{(\text{Li})} = 2.467 \text{ MeV}$  and spin-party  $\frac{3}{2}$ . The first excited state has a binding energy  $B_1^{(\mathrm{Li})} = 1.989$  MeV and spin-parity assignment  $\frac{1}{2}^-$ . These two p-wave states of the  $\frac{1}{2}^+$  <sup>3</sup>H and  $0^+$   $\alpha$  are included in the theory. The higher excited states with the same quantum numbers lie at least about 6 MeV above the  ${}^{3}\text{H-}\alpha$  threshold. These are not included in the lowenergy theory. The neutron separation energy of  ${}^{3}{\rm H}$  ( $\sim 6$ MeV) is identified with the high energy theory, and so <sup>3</sup>H is treated as a point-like fundamental particle along with the  $\alpha$ . The main differences between the EFT expressions for the  ${}^{3}\text{He}(\alpha,\gamma){}^{7}\text{Be}$  and  ${}^{3}\text{H}(\alpha,\gamma){}^{7}\text{Li}$  cross sections are the charges of the nuclei, and the relevant masses and binding energies. The separation between the low and high energy is smaller in the  ${}^{3}\text{H-}\alpha$  system which would result in a slower convergence of the  $Q/\Lambda$  expansion.

The total cross section for both the capture reactions is given as [2]:

$$\sigma(p) = \frac{1}{16\pi M^2} \frac{1}{2} \left[ \frac{p^2 + \gamma_1^2}{2\mu p} |M^{(^2P_{1/2})}|^2 + \frac{p^2 + \gamma_0^2}{2\mu p} |M^{(^2P_{3/2})}|^2 \right], \quad (1)$$

at center-of-mass (cm) relative momentum p of the incoming particles. We use the spectroscopic notation  $^{2s+1}L_j$  to indicate the capture to the  $^2P_{3/2}$  ground state with binding momentum  $\gamma_0=\sqrt{2\mu B_0}$ , and the  $^2P_{1/2}$  first excited state with binding momentum  $\gamma_1=\sqrt{2\mu B_1}$ .  $M=M_\psi+M_\phi$  is the total mass, and  $\mu=M_\psi M_\phi/M$  is the reduced mass of the incoming particles.  $M_\phi$  is the scalar  $0^+$   $\alpha$  mass, and  $M_\psi$  is the fermion  $\frac{1}{2}^+$   $^3$ He or  $^3$ H

mass as appropriate. The squared amplitude is given by

$$|M^{(\zeta)}|^2 = (2j+1) \left( \frac{Z_{\phi} M_{\psi}}{M} - \frac{Z_{\psi} M_{\phi}}{M} \right)^2 \times \left[ |\mathcal{A}(p)|^2 + 2|Y(p)|^2 \right] \frac{64\pi \alpha_e M^2([h^{(\zeta)}]^2 \mathcal{Z}^{(\zeta)})}{\mu} , \quad (2)$$

where  $\zeta={}^2P_{3/2}$  for the ground state (j=3/2) and  $\zeta={}^2P_{1/2}$  for the exited state (j=1/2).  $Z_\phi=2$  is the charge of the  $\alpha$  and  $Z_\psi$  is the charge of either the  ${}^3{\rm H}$  or the  ${}^3{\rm H}$  particle.  $\alpha_e=e^2/(4\pi)\approx 1/137$  is the fine structure constant. The capture from initial s- and d-wave states are given by the amplitudes  $\mathcal{A}(p)$  and Y(p) shown in the Appendix, Eq. (A1) and Eq. (A8) respectively. The factor  $([h^{(\zeta)}]^2\mathcal{Z}^{(\zeta)})$  is associated with the normalization of the outgoing  ${}^7{\rm Be}$  or  ${}^7{\rm Li}$  particle wave function, shown in Appendix, Eq. (B1). They are related to the asymptotic normalization constant (ANC) as:

$$C_{1, \zeta}^{2} = \frac{[\gamma^{(\zeta)}]^{2} [\Gamma(2 + k_{C}/\gamma^{(\zeta)})]^{2}}{\pi} [h^{(\zeta)}]^{2} \mathcal{Z}^{(\zeta)}.$$
 (3)

The ANCs depend on the binding momentum and the effective range  $\rho_1$  of the corresponding p-wave elastic channel of the outgoing  $^7\text{Be}$  or  $^7\text{Li}$  state.

The S-factor is calculated as a function of the c.m. incoming kinetic energy  $E=p^2/(2\mu)$  from the cross section as  $S_{34}(E)=Ee^{2\pi\eta_p}\sigma(p=\sqrt{2\mu E})$  where  $\eta_p=\alpha_e Z_\psi Z_\phi \mu/p$  is the Sommerfeld parameter.

## III. BAYESIAN PARAMETER ESTIMATION AND MODEL COMPARISON

In the EFT calculation we have several unknown couplings and parameters that we wish to constrain from available data. Suppose we represent the set of unknown couplings and parameters by the vector  $\boldsymbol{\theta}$  in the multi-dimensional parameter space. In the frequentist approach, the parameters  $\boldsymbol{\theta}$  are determined by maximizing the likelihood function

$$P(D|\boldsymbol{\theta}, H) = \prod_{i=1}^{N} \frac{1}{\sigma_i \sqrt{2\pi}} \exp\left\{-\frac{[y_i - \mu_i(\boldsymbol{\theta})]^2}{2\sigma_i^2}\right\}, \quad (4)$$

where the data set D consists of the N measurements  $y_i$  with corresponding measurement errors  $\sigma_i$ .  $\mu_i(\boldsymbol{\theta})$  are the theory predictions. The likelihood function gives the conditional probability of the data set D to be true given the parameters  $\boldsymbol{\theta}$  and the proposition H. Background information, theoretical assumptions, and hypothesis are included in the proposition H. Maximizing the likelihood function minimizes the  $\chi^2 \propto -\ln P(D|\boldsymbol{\theta}, H)$ .

In Bayesian analysis, the question one wants to answer is how probable some parameter value  $\theta$  given the data D. The answer is contained in the posterior probability distribution given by

$$P(\boldsymbol{\theta}|D,H) = \frac{P(D|\boldsymbol{\theta},H)P(\boldsymbol{\theta}|H)}{P(D|H)},$$
 (5)

where  $P(\boldsymbol{\theta}|H)$  is the prior distribution of the parameters which is predicated on the theoretical assumptions that is made in proposition H. The prior distribution is where one can, for example, include EFT assumptions about the expected sizes of the unknown couplings and parameters. The evidence P(D|H) is also known as the marginal likelihood because

$$P(D|H) = \int \prod_{i} d\theta_{i} P(D|\boldsymbol{\theta}, H) P(\boldsymbol{\theta}|H), \qquad (6)$$

comes from marginalizing the likelihood on the parameters. We used  $\int \prod_i d\theta_i P(\boldsymbol{\theta}|D,H) = 1$  above for normalized probabilities.

Parameter estimation from the posterior distribution in Eq. (5) does not require evaluation of the overall normalization factor, the evidence P(D|H). Markov chain Monte Carlo (MCMC) algorithms such as Metropolis-Hastings or some variation of it can be used to generate the posterior distribution  $P(D|\theta,H)P(\theta|H)$ . Each sample in the MCMC simulation represents a point in the multi-dimensional parameter space. The calculation of the marginalized probability distribution of a parameter say  $\theta_1$ 

$$P(\theta_1|D, H) = \int \prod_{i \neq 1} d\theta_i P(\boldsymbol{\theta}|D, H), \qquad (7)$$

is straightforward: just look at the distribution of the coordinate  $\theta_1$  in the sample which trivially corresponds to summing over all the other coordinates [19].

Model comparison in Bayesian analysis requires calculating the relevant evidences. In  $\chi^2$  minimization, one might get a better fit by including extra parameters. However, in Bayesian analysis there is a cost associated with including extra parameter as it introduces another prior distribution. The probability ratio of model A  $(M_A)$  and model B  $(M_B)$ , for a data set D, is given by the posterior odds ratio:

$$\frac{P(M_A|D,H)}{P(M_B|D,H)} = \frac{P(D|M_A,H)}{P(D|M_B,H)} \times \frac{P(M_A|H)}{P(M_B|H)}.$$
 (8)

The first factor on the right is just the ratio of evidences for  $M_A$  and  $M_B$ . The second factor is called the prior odds. In our analysis, we compare expressions from two different EFT power countings, not models, though we still refer to these as models, Appendix E. We set the prior odds to 1 when the two EFT expressions have similar accuracies in reproducing low energy properties such as binding energies, ANCs, etc., as detailed in Appendix E.

The evidence calculation requires numerical integration in the multi-dimensional parameter space. If we label the parameters of  $M_A$  by the vector  $\boldsymbol{\alpha}$ , and the parameters of  $M_B$  by the vector  $\boldsymbol{\beta}$ , then the evidences

are:

$$P(D|M_A, H) = \int \prod_i d\alpha_i P(D|\boldsymbol{\alpha}, M_A, H) P(\boldsymbol{\alpha}|M_A, H),$$

$$P(D|M_B, H) = \int \prod_i d\beta_i P(D|\boldsymbol{\beta}, M_B, H) P(\boldsymbol{\beta}|M_B, H).$$
(9)

The difficult task of calculating the evidences in the multi-dimensional parameter space is made easier in the Nested Sampling (NS) method introduced by Skilling [20]. The basic idea is to draw a set of  $n_{live}$  points randomly from the prior distribution  $P(\theta, H)$ , and arrange them from best to worst in terms of the likelihood function. Then one discards the worst point, and replaces it with another point from the prior distribution with the condition that it has a larger likelihood value. This guarantees that progressively higher likelihood regions of the parameter space is probed. In the original work by Skilling, at every iteration the worst point was replaced by Monte Carlo update using the Metropolis-Hastings algorithm. There has been a lot of algorithmic development since then on how to update the list of points, see review article [19]. We tried several of these methods. For our expressions, these methods disagree by about  $\sim 2$ in the calculation of  $\ln[P(M_A|D,H)/P(M_B|D,H)]$ , and we assume this level of systematic errors in model comparisons. We decided to use the MultiNest algorithm [21] implemented in Python [22]. We cross checked the numbers with our own Fortran code using the original NS algorithm [20].

# IV. S-FACTOR ESTIMATION FOR $^3{\rm He}(\alpha,\gamma)^7{\rm Be}$ AND $^3{\rm H}(\alpha,\gamma)^7{\rm Li}$

The cross section (and the related S-factor) expressions for  ${}^{3}\text{He}(\alpha,\gamma){}^{7}\text{Be}$  and  ${}^{3}\text{H}(\alpha,\gamma){}^{7}\text{Li}$  are given by Eq. (1). It depends on the amplitudes  $\mathcal{A}(p)$  and Y(p). The latter is expressed in Eq. (A8) without any unknown parameters. The former depends on the initial state strong interaction s-wave phase shift  $\delta_0$  that can be written model-independently in terms of scattering parameters: scattering length  $a_0$ , effective range  $r_0$ , shape parameter  $s_0$ , etc., in Eq (A4). We keep only three swave scattering parameters  $a_0$ ,  $r_0$  and  $s_0$  in our analysis.  $\mathcal{A}(p)$  also depends on 2 two-body current couplings  $L_{\mathrm{E}1}^{(\zeta)}$ for  $\zeta = {}^{2}P_{3/2}$ ,  $\zeta = {}^{2}P_{1/2}$ . The cross section is multiplied by the overall factor  $([h^{(\zeta)}]^2 \mathcal{Z}^{(\zeta)})$ , Eq. (B1), that depends on the binding momenta  $\gamma$  and the effective ranges  $\rho_1$  in the p-wave channels  ${}^{2}P_{3/2}$  and  ${}^{2}P_{1/2}$ . This amounts to 7 parameters/couplings for the capture cross section as we take the binding momenta as given. We use the notation  $\pm$  to indicate the  ${}^{2}P_{3/2}$  and  ${}^{2}P_{1/2}$  channels, respectively.

A  $\chi^2$  fit to capture data [2] for  ${}^3{\rm He}(\alpha,\gamma)^7{\rm Be}$  does not constraint the p-wave effective ranges  $\rho_1^{(\pm)}$  accurately. The wave function normalization constants  $[h^{(\pm)}]^2 \mathcal{Z}^{(\pm)}$ 

have poles at approximately  $\rho_1^{(+)} = -47.4$  MeV and  $\rho_1^{(-)} = -32.4$  MeV, respectively. A small change in the effective range values changes the normalization of the cross section significantly. Moreover, one finds that for the parameters from the  $\chi^2$  fit, there is a large cancellation among the terms in  $\mathcal{A}(p)$  such that the two-body contribution becomes important. However, the contribution from the two-body currents can be suppressed by choosing the effective range contribution near the pole in  $([h^{(\zeta)}]^2\mathcal{Z}^{(\zeta)})$ . Therefore, we find it important to include information from p-wave elastic phase shifts  $\delta_1^{(\pm)}$  to constraint  $\rho_1^{(\pm)}$  more accurately. This entails including the shape parameters  $\sigma_1^{(\pm)}$  in the fit.  $\sigma_1^{(\pm)}$  contributes to phase shifts  $\delta_1^{(\pm)}$  but not to the capture cross section. The total parameters to be fit now increases to 9:  $a_0, r_0, s_0, \rho_1^{(\pm)}, \sigma_1^{(\pm)}, L_{\mathrm{E1}}^{(\pm)}$ .

We start with the new analysis of  ${}^{3}\text{He}(\alpha, \gamma)^{7}\text{Be}$  [2]. The capture and elastic scattering data is more accurately known for this reaction than for  ${}^{3}\text{H}(\alpha, \gamma)^{7}\text{Li}$ .

## A. Capture reaction ${}^{3}\text{He}(\alpha, \gamma)^{7}\text{Be}$

We use charge  $Z_{\psi}=2$ , mass  $M_{\psi}=2809.41$  MeV for the incoming  $^3$ He, and charge  $Z_{\phi}=2$ , mass  $M_{\phi}=3728.4$  MeV for the incoming  $\alpha$  in Eq. (1). The  $^3$ He( $\alpha,\gamma$ ) $^7$ Be capture data are from ERNA [7], LUNA [8], Notre Dame [9], Seattle [10], and Weizmann [11]. It includes prompt photon, activation and recoil (ERNA) measurements. For the prompt data, the branching ratio  $R_0$  of capture to the excited state to the ground state is available.

In the Bayesian analysis we explore fits to capture data up to c.m. energy (momentum)  $E \lesssim 1$  MeV ( $p \lesssim 60$  MeV) that we call region I. Fits to capture data over  $E \lesssim 2$  MeV ( $p \lesssim 80$  MeV) we call region II. The phase shift data for  $\delta_0$ ,  $\delta_1^{(\pm)}$  is from an old source [23] that was analyzed by Boykin et al. in Ref. [24]. The phase shift data starts from around  $E \sim 2$  MeV ( $p \sim 80$  MeV), which is at the higher end of the range of applicability of the EFT. We fit with phase shift data, and also without (indicated by an asterisk \* as appropriate). In all, we have four combinations of data sets for the fits. Region I includes 42 S-factor data and 20  $R_0$  data points whereas region II includes 70 S-factor data and 32  $R_0$  data points. The phase shifts include 10 data points in each of the three channels.

In the EFT, the momentum  $p \sim 70$  MeV and final state binding momenta  $\gamma_0 \sim \gamma_1 \sim 60\text{--}70$  MeV constitutes the small scale Q. The pion mass, excited states of  $^3\mathrm{He}$ ,  $\alpha$ , etc., constitutes the cutoff scale  $\Lambda \gtrsim 150\text{--}200$  MeV. In the s-wave capture amplitude  $\mathcal{A}(p)$ , Eq. (A1), the first term X(p) that only contains Coulomb interaction is O(1) at small momentum. The rest of the contributions, at arbitrarily small momentum p, scales as  $a_0(B+\mu J_0)/\mu^2$  and  $a_0k_0L_{\mathrm{E1}}^{(\zeta)}$ . The linear combination

 $(B+\mu J_0)/\mu^2$  scales as  $Q^3/\Lambda^2$ , and the photon energy  $k_0=(p^2+\gamma^2)/(2\mu)\sim Q^3/\Lambda^2$  [2, 25]. Thus at low momentum the contributions from initial state strong interaction  $a_0(B+\mu J_0)/\mu^2\sim a_0Q^3/\Lambda^2$ . The two-body current contribution  $a_0k_0L_{\rm E1}^{(\zeta)}\sim a_0Q^3/\Lambda^2$  for a natural sized dimensionless coupling  $L_{\rm E1}^{(\zeta)}\sim 1$ . The size of the s-wave scattering length then determines the relative contributions in the amplitude at low momentum.

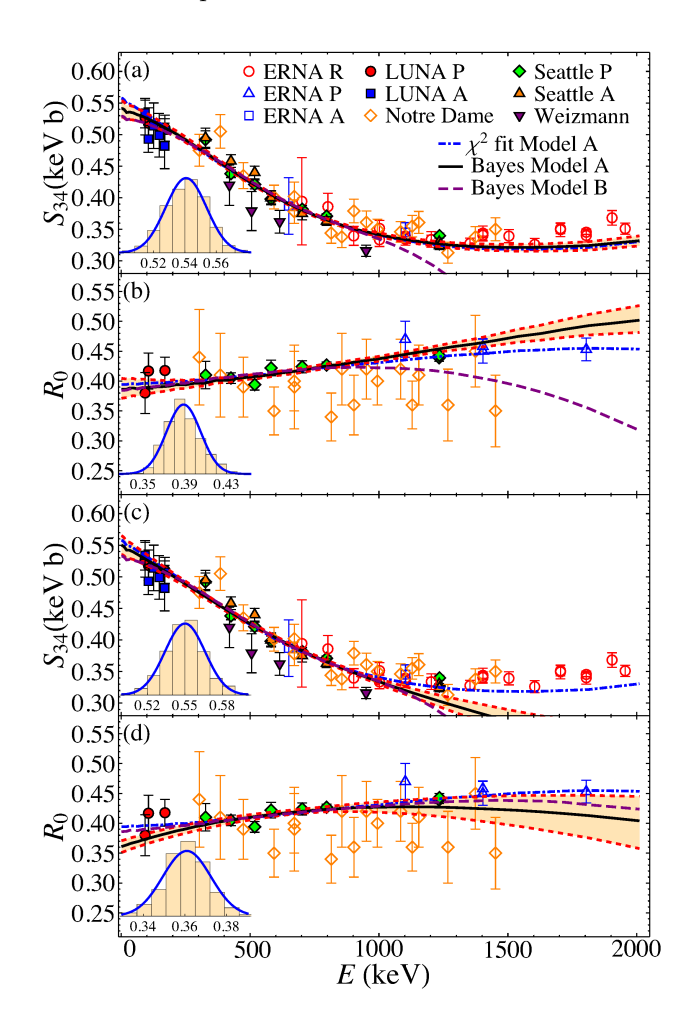


FIG. 1.  $^3\mathrm{He}(\alpha,\gamma)^7\mathrm{Be}$ : Model comparison for capture cross section. Solid (black) curve is the median result using Model A. The shaded region, bounded by the dashed (red) curves, represents 68% of the posterior distribution. The long-dashed (purple) curve is for Model B. We include the  $\chi^2$  result as dot-dashed (blue) curve for comparison. Panel (a) and (b) are simultaneous fits to capture and phase shift data. Panel (c) and (d) are fits only to capture data. These fits are to capture data in region I,  $E\lesssim 1000$  keV. The inset shows the distribution for Model A at  $E_\star=60\times 10^{-3}$  keV.

 $\chi^2$  minimization that included two-body current contribution gave a large  $a_0\sim 20\text{--}30~\text{fm}\sim \Lambda^2/Q^3,$  and consequently the initial state interactions  $a_0(B+\mu J_0)/\mu^2\sim 1$  and two-body currents  $a_0k_0L_{\rm E1}^{(\zeta)}\sim 1$  are LO contributions.  $\chi^2$  minimization without two-body currents give a

smaller  $a_0 \sim 5-10$  fm  $\sim \Lambda/Q^2$  [2]. This will make initial state interaction  $a_0(B+\mu J_0)/\mu^2 \sim Q/\Lambda$  a NLO contribution. In EFT, there is always going to be two-body currents unless some symmetry prevents them. Then the only consideration is at what order in perturbation they contribute. Again assuming natural sized couplings  $L_{\rm E1}^{(\zeta)} \sim 1$ , the two-body contribution  $a_0 k_0 L_{\rm E1}^{(\zeta)} \sim Q/\Lambda$  is also a NLO effect for  $a_0 \sim \Lambda/Q^2$ .

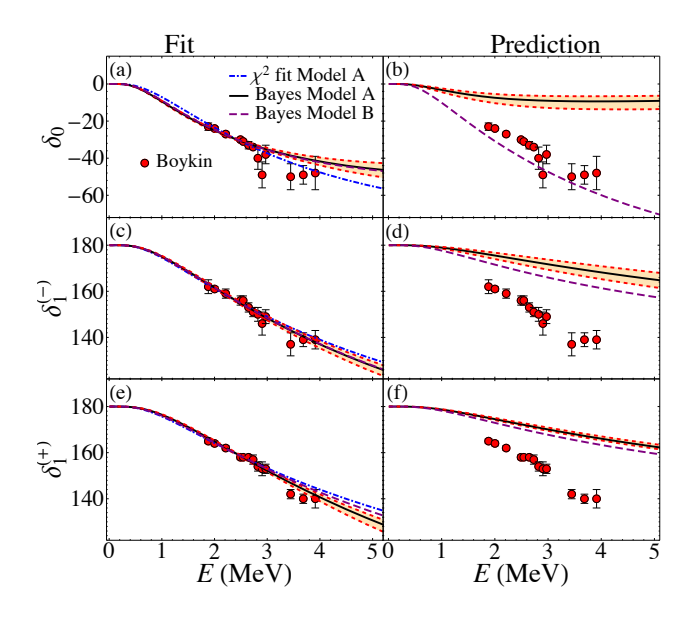


FIG. 2.  ${}^{3}\text{He}(\alpha,\gamma){}^{7}\text{Be}$ : Model comparison for scattering phase shifts. Notation for the curves the same as in Fig. 1. Panels on the left are fits to phase shifts, and the panels on the right are predictions as discussed in the text.

We consider two power countings. The first one, proposed in Ref.[2], assumes a large  $a_0 \sim \Lambda^2/Q^3$ . This we call "Model A" though EFT is a model-independent formulation. In this power counting, detailed in Ref. [2], the other parameters and couplings scale as  $r_0 \sim 1/\Lambda$ ,  $s_0 \sim 1/\Lambda^3$ ,  $\rho_1^{(\pm)} \sim Q$ ,  $\sigma_1^{(\pm)} \sim 1/\Lambda$ ,  $L_{\rm E1}^{(\pm)} \sim 1$ . The capture cross section depends on  $a_0$ ,  $r_0$ ,  $\rho_1^{(\pm)}$ ,  $L_{\rm E1}^{(\pm)}$  at LO. The NLO contribution gets an additional contribution from  $s_0$ . The s-wave phase shift  $\delta_0$  depends on  $a_0$  and  $r_0$  at LO, and at NLO brings in  $s_0$ . Though for a natural sized  $r_0 \sim 1/\Lambda$  the effective range contribution scales as expected  $r_0 p^2 \sim Q^2/\Lambda$ , there is a large cancellation in the linear combination  $r_0 p^2/2 - 2k_C H(\eta_p) \sim Q^3/\Lambda^2$  in the region of strong Coulomb interaction. Thus this contribution is of similar size to the scattering length contribution  $1/a_0 \sim Q^3/\Lambda^2$  that enters at LO [2].

In the second power-counting that we call "Model B", one assumes a smaller  $a_0 \sim \Lambda/Q^2$ . The rest of the parameters have the same scaling as Model A. However, the perturbative expansion is now different. The LO capture cross section has no initial state strong interaction. It only depends on  $\rho_1^{(\pm)}$ .  $a_0$  and  $L_{\rm E1}^{(\pm)}$  contributes at NLO, and the linear combination  $r_0p^2/2 - 2k_CH(\eta_p)$  at next-

to-next-to-leading order (NNLO). In phase shift  $\delta_0$ ,  $a_0$  contributes at LO,  $r_0$  at NLO and  $s_0$  at NNLO. The p-wave phase shift contributions remain unchanged from Model A above. The d wave contribution Y(p) is now included at NNLO.

Model A and Model B are compared by calculating the posterior odds ratio  $P(M_A|D,H)/P(M_B|D,H)$  from Eq. (8). The two power countings differ at LO from each other and also from the "true" value. As one includes higher order corrections, these two theories (if they are valid theories) are expected to converge to the true value at different rates. Naïvely the expansion is in powers of  $Q/\Lambda$ . However, the actual functional dependence on  $p/\Lambda$ in Model A and Model B are different which would lead to different rates of convergence over the momentum range we consider. Thus Model A and Model B have different accuracies and precisions (higher order corrections) at each order of the expansion. We chose to compare them at the same level of accuracy instead of the same level of precision even though it leads to comparing the two theories at different orders of the perturbative  $Q/\Lambda$ expansion. Comparing the two at the same order of expansion would achieve neither the same level of accuracy nor the same level of precision. We explain the details in Appendix E.

In our analysis, the  $\chi^2$  for the fit without two-body currents was larger than the one with two-body currents when phase shift data, especially  $\delta_0$ , was used. We explore the possibility that the uncertainty in the phase shifts are actually larger than estimated. We consider  $\sigma^2 \to K^2 + \sigma^2$  to describe an unaccounted noise. We draw K from the uniform distribution  $U(0^{\circ}, 10^{\circ})$ . We also consider the possibility  $\sigma^2 \to K^2 \sigma^2$  with K drawn from U(1,10). Both of these give similar fits so we present the analysis for  $K^2 + \sigma^2$  only. Note that the errors  $\sigma$  in the phase shift data are estimated to be around  $\sim 1^{\circ}-3^{\circ}$  [24]. Alternatively, one could also explore the possibility of an uncertainty in the overall normalization of the phase shift measurements. As the s and p wave phase shifts are from the same measurement and analysis, we did not consider the possibility of introducing separate measurement errors for the different elastic scattering channels. We use the following uniform prior distributions for the parameters and couplings in the EFT expressions:

$$\begin{split} a_0 &\sim U(1~\text{fm}, 70~\text{fm})\,, \\ r_0 &\sim U(-5~\text{fm}, 5~\text{fm})\,, \\ s_0 &\sim U(-30~\text{fm}^3, 30~\text{fm}^3)\,, \\ \rho_1^{(+)} &\sim U(-300~\text{MeV}, -48~\text{MeV})\,, \\ \rho_1^{(-)} &\sim U(-300~\text{MeV}, -33~\text{MeV})\,, \\ \sigma_1^{(\pm)} &\sim U(-5~\text{fm}, 5~\text{fm})\,, \\ L_1^{(\pm)} &\sim U(-10, 10)\,, \\ K &\sim U(0^\circ, 10^\circ)\,. \end{split}$$

Fits without phase shifts do not depend on  $\sigma_1^{(\pm)}$  and K. Model B without phase shift data also does not depend

on  $s_0$ . The range for each of the uniform distributions above was guided by EFT power counting estimates. The ranges were wide enough that about 95% of the posterior distributions of the parameters and couplings are not pressed against the boundaries. For certain parameters such as the p-wave effective ranges  $\rho_1^{(\pm)}$  physical constraint that the ANCs be positive determines the upper bounds. All these assumptions are considered part of the background information in the proposition H in the probability distributions.

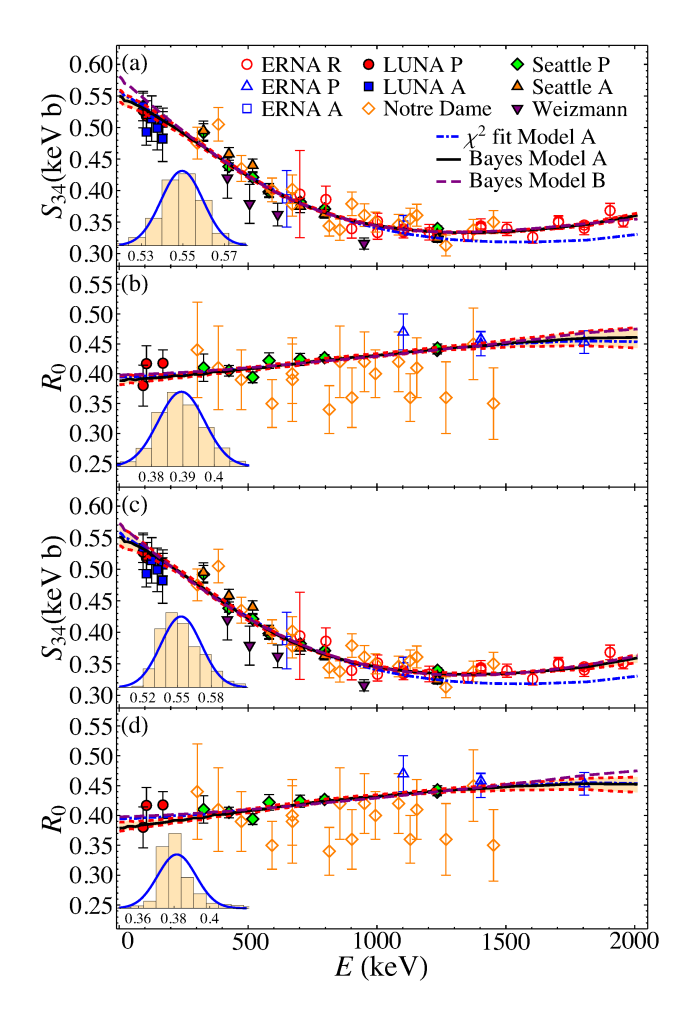


FIG. 3.  $^3{\rm He}(\alpha,\gamma)^7{\rm Be}$ : Model comparison for capture cross section. Notations the same as in Fig. 1. The fits included capture data in region II,  $E\lesssim 2000~{\rm keV}$ .

In Figs. 1 and 2, we present fits in region I with and without phase shifts. In Fig. 1, the upper panels (a) and (b) are fits with phase shift data, and the lower panels (c) and (d) are without. The panels on the left in Fig. 2 are fits to phase shift data. The ones on the right are phase shift predictions from capture data. We include the  $\chi^2$  fit of Model A to data in region I (with phase shift) for comparison [2]. The parameter estimates are in table V. The Bayesian curves are drawn from the posterior distributions of the parameter

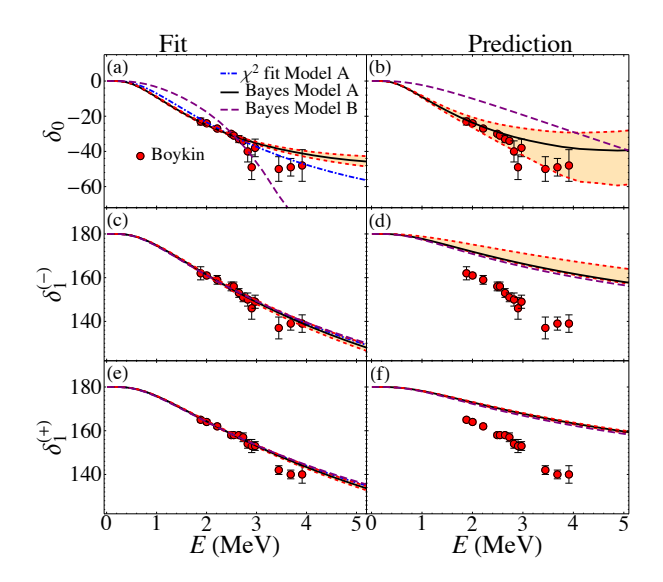


FIG. 4.  $^3{\rm He}(\alpha,\gamma)^7{\rm Be}$ : Model comparison for scattering phase shifts: Notations the same as in Fig. 2 but with capture data in region II  $E\lesssim 2000~{\rm keV}$ .

eters, not directly from the median values from the table. The posterior odds for the fit with phase shift is  $\ln[P(M_A|D,H)/P(M_B|D,H)] \approx 2.6\pm0.8^1$  slightly favoring Model A, though the odds are similar if one accounts for systematic error. For the fit without phase shift data  $\ln[P(M_A^*|D,H)/P(M_B^*|D,H)] \approx 4.9\pm0.6$  is largely in favor of model A. We remind the reader that the asterisk \* indicates fits without phase shift data. From Fig. 1 panel (a), we see Model A (with phase shift) reproduces capture data in region II better than the other fits though it was fitted only to region I data. Note that Model B fit parameters are not consistent with the EFT power counting where we expected a smaller  $a_0$ , see table V.

Figs. 3 and 4 represent a similar analysis but fitted to capture data in region II. The parameter estimates are in table V. The posterior odds are  $\ln[P(M_A|D,H)/P(M_B|D,H)] \approx 31.6 \pm 0.9$  and  $\ln[P(M_A^*|D,H)/P(M_B^*|D,H)] \approx 0.2 \pm 0.8$ . These fits indicate that Model B is not able to reproduce both phase shift and capture data simultaneously over a large region. The large K value in table V for Model B II corroborates this. Without constraint from phase shift, model A\* II and model B\* II are equally favored.

The posterior distributions for the parameters for the fits that are consistent with the EFT power counting are

<sup>&</sup>lt;sup>1</sup> The numerical errors in the evidence calculations arise from the MCMC algorithm. In NS it is estimated from the information gain  $\mathcal{H} = \int \prod_i d\theta_i \frac{P(D|\boldsymbol{\theta},H)}{P(D|H)} P(\boldsymbol{\theta}|H) \log \frac{P(D|\boldsymbol{\theta},H)}{P(D|H)}$  as  $\sqrt{\mathcal{H}/n_{\text{live}}}$  where  $n_{\text{live}}$  is the number of live points, Appendix D. The multi-dimensional integration in NS is done through a change of variable  $\prod_i d\theta_i P(\boldsymbol{\theta}|H) = dx$  where the likelihood is a decreasing function of  $x \in [0,1]$  with the least likelihood at x=1. The integration in x is done probabilistically as described in Ref. [20].

shown in Appendix D. We see correlation say in fits A I (Figs. 9) and A II (Figs. 10) between  $\rho_1^{(\pm)}$  and  $L_1^{(\pm)}$  in Model A supporting the earlier observation [2]. One also sees the correlation between scattering parameters  $r_0$ - $s_0$ ,  $\rho_1^{(\pm)}$ - $\sigma_1^{(\pm)}$  get less pronounced going from A I to A II as one fits to capture cross section over a larger momentum region. This is expected. The phase shift data is available only in a small region of validity of the EFT, which prevents clearly separating the effective range and shape parameter effect. As one explores a larger momentum capture cross section region, the effect of the two are better separated. In Model B, we do not expect to see large correlation between  $\rho_1^{(\pm)}$  and  $L_1^{(\pm)}$  because the effective ranges appear at LO whereas the two-body currents appear pear at NLO. The difference in correlation between  $\rho_1^{(\pm)}$ and  $L_1^{(\pm)}$  in fit A II (Fig. 10) and B II (Fig 12) is clear. Low-energy phase shifts from  ${}^{3}\text{He-}\alpha$  elastic scattering experiments as those planned at TRIUMF [26] would help remove some of the correlations in scattering parameters.

## B. Capture reaction ${}^{3}\mathrm{H}(\alpha,\gamma){}^{7}\mathrm{Li}$

In the  ${}^3{\rm H}(\alpha,\gamma){}^7{\rm Li}$  calculation we use  $Z_\psi=1$  and mass  $M_\psi=2809.43$  MeV for the incoming  ${}^3{\rm H}$ . The charge and mass for the  $\alpha$  is the same as before. The data for the capture cross section are from Caltech [14] and Tomsk [15]. As in the case of  ${}^7{\rm Be}$ , if we associate the binding momenta for the ground and 1st excited of  ${}^7{\rm Li}$   $\gamma_0\sim\gamma_1\sim80$ –90 MeV with the scale Q, then for this system we expect the convergence to be slower compared to the previous  ${}^3{\rm He}$ - $\alpha$  system which had smaller  $\gamma_0,\gamma_1$ .

The role of the initial state interaction and the two-body current contributions are predicated on the size of the s-wave scattering length  $a_0$  as before. However, in this system a larger  $a_0 \sim \Lambda^2/Q^3$  corresponds to only  $\sim 10\text{--}20$  fm. A smaller  $a_0 \sim \Lambda/Q^2 \sim 1\text{--}5$  fm. The larger  $a_0$  would make the initial state strong interaction and two-body current contributions LO, and the smaller  $a_0$  would make these contributions NLO. The power-counting arguments for  $^3\mathrm{H}(\alpha,\gamma)^7\mathrm{L}$ i are similar to the  $^3\mathrm{He}(\alpha,\gamma)^7\mathrm{Be}$  capture. The difference is that now Q is numerically larger.

The phase shift information of the initial  $^3\text{H-}\alpha$  state is less well known than the  $^3\text{He-}\alpha$  state. We digitized the s-wave phase shift  $\delta_0$  for momentum range  $p\sim70$ –90 MeV from Fig. 15 in Ref. [23]. The p waves appear very noisy and we decided not to use these in the fits. The authors estimated an error of about 5° in the phase shift analysis for  $^3\text{He-}\alpha$  but the errors in the  $^3\text{H-}\alpha$  phase shifts are not listed. We find a mention of 3% systematic error in  $^3\text{H-}\alpha$  that we use [23]. It is likely the error in this system is similar to  $^3\text{He-}\alpha$ . We add an additional noise as before and use  $K^2+\sigma^2$  in the fits with  $K\sim U(0^\circ,10^\circ)$ . We use

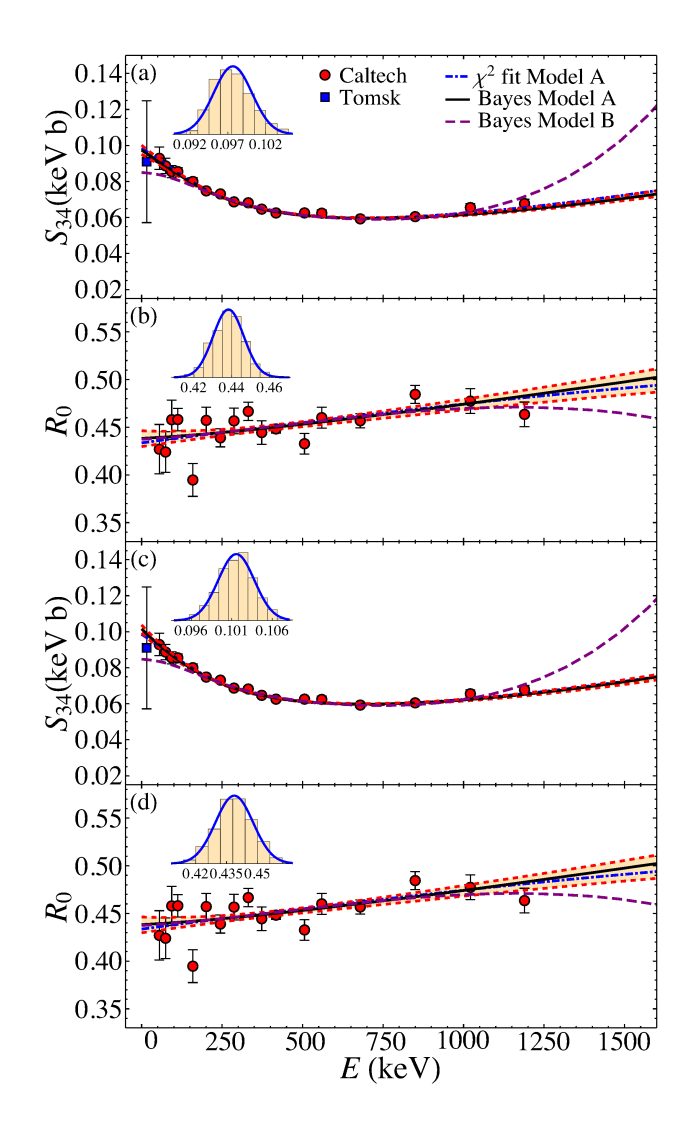


FIG. 5.  ${}^{3}\text{H}(\alpha,\gamma)^{7}\text{Li}$ : Model comparison for capture cross section. Solid (black) curve is the median result using Model A. The shaded band around it, bounded by the dashed (red) curves, represents 68% of the posterior distribution. The long-dashed (purple) curve is for Model B. The dot-dashed (blue) curve is for  $\chi^{2}$  fit. The inset shows Model A at  $E_{\star}$ .

the following priors:

$$a_0 \sim U(1 \text{ fm}, 70 \text{ fm}),$$
  
 $r_0 \sim U(-5 \text{ fm}, 5 \text{ fm}),$   
 $s_0 \sim U(-45 \text{ fm}^3, 45 \text{ fm}^3),$   
 $\rho_1^{(+)} \sim U(-320 \text{ MeV}, -126 \text{ MeV}),$   
 $\rho_1^{(-)} \sim U(-320 \text{ MeV}, -106 \text{ MeV}),$   
 $L_1^{(\pm)} \sim U(-10, 10),$   
 $K \sim U(0^{\circ}, 10^{\circ}).$  (11)

The fits do not depend on the *p*-wave shape parameters  $\sigma_1^{(\pm)}$  since we do not use the *p*-wave phase shifts. The upper limits on the effective ranges  $\rho_1^{(\pm)}$  are constrained

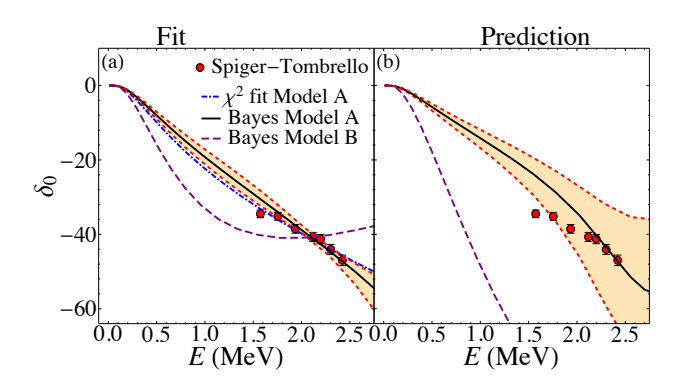


FIG. 6.  ${}^{3}\text{H}(\alpha,\gamma){}^{7}\text{Li}$ : Model comparison for scattering phase shifts. Notation for the curves the same as in Fig. 5. The panel on the left is fit to phase shift data whereas the panel on the right are predictions.

by requiring positive ANCs. We use 18 S-factor  $S_{34}$  data, 17 branching ratio  $R_0$  data and 7 phase shift  $\delta_0$  data points for the fits.

Figs. 5 and 6 shows the Bayesian fits. The power counting for Model A and Model B are the same as in  ${}^3{\rm He}(\alpha,\gamma){}^7{\rm Be}$ . We include a  $\chi^2$  fit with phase shift using Model A for comparison. The upper panels (a) and (b) of Fig. 5 are for fits with s-wave phase shift, and the lower panels (c) and (d) are without. Fig. 6, left panel are fits to phase shift whereas the right panel are the predictions from fits to capture data. The posterior odds overwhelmingly favor Model A with  $\ln[P(M_A|D,H)/P(M_B|D,H)] \approx 19.7 \pm 0.7$ ,  $\ln[P(M_A^*|D,H)/P(M_B^*|D,H)] \approx 18.4 \pm 0.6$ . The parameter estimations are in table VI. The fits to phase shift suggests errors of about 5° in  $\delta_0$ . Model B fits are not consistent with the EFT power counting as we expected a smaller  $a_0$ , see table VI.

The posterior distributions for the Model A fit parameters is shown in Appendix D as only Model A is a consistent EFT for this system. We see the expected correlations between  $\rho_1^{(\pm)}$  and  $L_1^{(\pm)}$ , Figs. 14, 15. Accurate low-energy phase shift data would help remove some of the correlations between the effective range parameters.

## V. DISCUSSION AND SUMMARY

We performed several analysis of the EFT cross sections for  ${}^{3}\text{He}(\alpha,\gamma){}^{7}\text{Be}$  and  ${}^{3}\text{H}(\alpha,\gamma){}^{7}\text{Li}$  to draw Bayesian inference. Two EFT power counting proposals were compared. Typically, LO cross sections in EFT do not depend on two-body currents. This allows one to perform capture calculations once a few LO couplings are determined from elastic scattering data if they are known. For the two capture reactions considered here, elastic scattering data is not well measured. Available data on elastic scattering in  ${}^{3}\text{He-}\alpha$  [23, 24] and  ${}^{3}\text{H-}\alpha$  [23] systems suggest the s-wave scattering lengths  $a_{0}$ s are fine tuned to

be large. This makes initial state interactions in the capture reactions dominant, and as a consequence the twobody currents could contribute at LO [2]. We called this EFT power counting Model A. Alternatively, one could have a power counting where two-body currents appear at higher order in the perturbation. This would require a smaller s-wave scattering length. We call this power counting Model B. If we ignore the poorly known elastic scattering data, then this second power counting can be used to describe the capture data. The relatively smaller initial state interaction contributions in Model B can be compensated by a larger wave function normalization constant which requires only small variation in the respective p-wave effective ranges as described earlier. We discuss the results of the analysis for  ${}^{3}\text{He}(\alpha,\gamma){}^{7}\text{Be}$  and  $^{3}$ H $(\alpha, \gamma)^{7}$ Li separately below.

## A. ${}^{3}\mathrm{He}(\alpha,\gamma){}^{7}\mathrm{Be}$

We present the 8 different fits used to draw Bayesian inference for this reaction. First we start with the fits in the smaller capture energy region I ( $E \lesssim 1000~{\rm keV}$ ). The posterior odds favored Model A both with and without phase shift data in the fits. However, if we also look at the overall trend then we see the data for S-factor  $S_{34}$  rises upward from around  $E \sim 1500~{\rm keV}$ . The Model A fit with phase shift, we call Model A I, best describes the capture data over the energy range  $E \lesssim 2000~{\rm keV}$ . We note that the Model B fits in this region are not self-consistent in that they suggest an  $a_0$  value larger than the power counting, table V.

In the fits to capture energy region II ( $E \lesssim 2000~{\rm keV}$ ), Model A with phase shift, we call Model A II, is favored over Model B by the posterior odds. For the fits without phase shifts, both Model A\* II and Model B\* II are equally favored by the posterior odds ratio. The asterisk \* indicates fits without phase shift data.

Fit	$S_{34}(E_{\star}) \; (\text{keV b})$	$S'_{34}(E_{\star}) \ (10^{-4} \ \mathrm{b})$
$\chi^2$	$0.558\pm0.008\!\pm\!0.056$	$-2.71 \pm 0.20 \pm 0.27$
Model A I	$0.541^{+0.012}_{-0.014} \pm 0.054$	$-1.34^{+0.64}_{-0.59} \pm 0.13$
Model A II	$0.550^{+0.009}_{-0.010} \pm 0.055$	$-2.00^{+0.36}_{-0.35} \pm 0.20$
Model A* II	$0.551^{+0.021}_{-0.014} \pm 0.055$	$-1.86^{+0.72}_{-1.69} \pm 0.19$
Model B* II	$0.573^{+0.007}_{-0.007} \pm 0.017$	$-3.72^{+0.11}_{-0.10} \pm 0.11$

TABLE I.  ${}^{3}\text{He}(\alpha,\gamma){}^{7}\text{Be}$ :  $S_{34}$  and  $S_{34}'$  at threshold (defined as  $E_{\star}=60\times10^{-3}$  keV). The second set of errors are estimated from the EFT perturbation as detailed in the text.

Tables I and II has the S-factors  $S_{34}$  and branching ratios  $R_0$ , respectively, for the 4 fits described above. We also include the  $\chi^2$  fit of Model A for comparison [2]. We include the derivative  $S'_{34}$  as well. All the numbers were evaluated at  $E_{\star} = 60 \times 10^{-3}$  keV. We include the estimated EFT errors. The NLO Model A results have a 10% error, and the NNLO Model B results have a 3% error.

Fit	$R_0$
$\chi^2$	$0.395 \pm 0.014 \pm 0.039$
Model A I	$0.387^{+0.018}_{-0.015} \pm 0.039$
Model A II	$0.389^{+0.008}_{-0.007} \pm 0.039$
Model A* II	$0.379^{+0.010}_{-0.005} \pm 0.038$
Model B* II	$0.401^{+0.005}_{-0.005} \pm 0.012$

TABLE II.  ${}^{3}\text{He}(\alpha, \gamma){}^{7}\text{Be}$ : Branching ratio  $R_{0}$  at threshold (defined as  $E_{\star} = 60 \times 10^{-3} \text{ keV}$ ). The second set of errors are estimated from the EFT perturbation as detailed in the text.

On the one hand these EFT errors are optimistic estimates where we used the smaller binding momentum  $\gamma_0$ for  $Q \sim 60$  MeV with the larger cutoff  $\Lambda \sim 200$  MeV. On the other hand, the actual theoretical errors at threshold in halo EFT might be smaller. The final state wave functions (ground and excited states of <sup>7</sup>Be) do not receive any higher order correction beyond the binding momentum  $\gamma$  and the effective range  $\rho_1$ , see Eq. (B1). The higher order initial state corrections and two-body currents beyond what was included here involve higher powers of momentum p (not Q) that would be suppressed at threshold. Magnetic transitions from initial p-wave states are known to be much smaller than the d-wave contributions we include [27]. We leave a more systematic theory error estimate within the Bayesian framework for future, see Refs. [28–30] and references therein. We provide more details in Appendix E regarding the calculating of cross sections at different orders of the expansion in Model A and Model B.

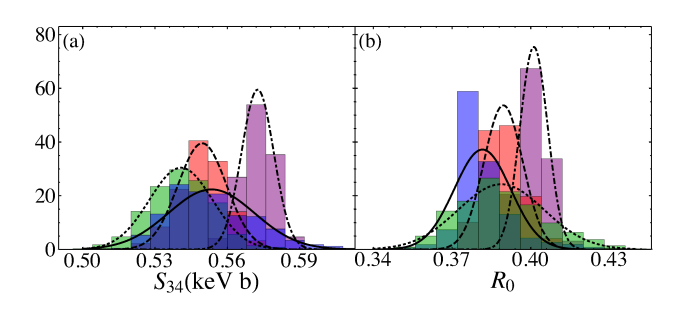


FIG. 7.  $^3{\rm He}(\alpha,\gamma)^7{\rm Be}$ : S-factor  $S_{34}$  and branching ratio  $R_0$  at threshold ( $E_\star=60\times10^{-3}$  keV). The posterior distributions for fits Model A I, Model A II, Model A\* II and Model B\* II are presented as green, red, blue and purple colored histograms, respectively. The corresponding Gaussian probability distributions are given by the dotted, dashed, solid and dot-dashed curves, respectively.

Fig. 7 shows the posterior distributions for the 4 S-factors and branching ratios from tables I and II. The symmetric distributions can be described with a Gaussian form shown by the various smooth curves unlike the skewed distributions as expected. The spread in some

of the quantities is related to the uncertainty in the parameter estimates, especially the p-wave effective ranges  $\rho_1^{(\pm)}$  for Model A fits, see table V. Large magnitude  $|\rho_1^{(\pm)}|$  makes the wave function normalization constant smaller which can be compensated by a larger two-body current  $L_1^{(\pm)}$  as the parameter estimates indicate. The planned TRIUMF  $^3$ He- $\alpha$  elastic scattering experiments and phase shift analysis at low energies  $E\gtrsim 500$  keV would be able to shed some light on this [26], and help establish the appropriate EFT power counting.

The EFT S-factor at threshold can be compared to other recent calculations such as - 0.593 keV b from FMD [31], 0.59 keV b from NCSM [32]; and evaluations such as  $-[0.580 \pm 0.043(\text{stat.}) \pm 0.054(\text{sys.})] \text{ keV}$ b from Cyburt-Davids [6],  $(0.57 \pm 0.04)$  keV b from ERNA [7],  $(0.567 \pm 0.018 \pm 0.004)$  keV b from LUNA [8],  $(0.554\pm0.020)$  keV b from Notre Dame [9],  $(0.595\pm0.018)$ keV b from Seattle [10], and  $(0.53 \pm 0.02 \pm 0.01)$  keV b from Weizmann [11]. We also compare to a recent EFT work using Bayesian inference [33] that finds at threshold  $S_{34}(0) = 0.578^{+0.015}_{-0.016}$  keV b and  $R_0(0) = 0.406^{+0.013}_{-0.011}$ . Ref. [33] only used capture data to draw their inferences. Looking at tables I and II, it would seem the results of Ref. [33] are more aligned with Model B\* II, though the exact power counting used the article is not clear. The "best" recommended value from the review in Ref. [1] is:  $S_{34}(0) = [0.56 \pm 0.02(\text{expt.}) \pm 0.02(\text{theory})] \text{ keV b.}$ 

From the various fits, we recommend the following: Model A II if we want to include phase shift information, and either Model A\* II or Model B\* II if no phase shift information is used. However, one has to keep in mind that in our analysis we allowed for an unaccounted noise in the phase shifts in addition to the reported measurement errors [24]. Thus one should not completely disregard the fits with phase shift data. Then, Model A II would be the preferred fit.

B.  $^{3}\text{H}(\alpha,\gamma)^{7}\text{Li}$ 

Fit	$S_{34}(E_{\star}) \; (\text{keV b})$	$S'_{34}(E_{\star}) \ (10^{-4} \ \mathrm{b})$
$\chi^2$	$0.098 \pm 0.003 \pm 0.016$	$-1.13 \pm 0.24 \pm 0.18$
Model A	$0.097^{+0.003}_{-0.002} \pm 0.016$	$-1.04^{+0.12}_{-0.20} \pm 0.17$
$\operatorname{Model} A^*$	$0.102^{+0.002}_{-0.002} \pm 0.016$	$-1.81^{+0.16}_{-0.15} \pm 0.29$

TABLE III.  $^3\mathrm{H}(\alpha,\gamma)^7\mathrm{Li}$ :  $S_{34}$  and  $S_{34}'$  at threshold (defined as  $E_\star = 60 \times 10^{-3}$  keV). The second set of errors are estimated from the EFT perturbation as detailed in the text.

To draw our Bayesian inferences, we performed 4 different fits in this system. Here the EFT power counting of Model A (with phase shift data) and Model A\* (without phase shift data) are favored. Moreover, the Model B and Model B\* fits are not consistent with the power counting estimate for the  $a_0$  values, table VI. The S-factors and

branching ratios are in tables III and IV. The corresponding posterior distributions, and the associated Gaussian forms are shown in Fig. 8. The fit without phase shift data gives a larger  $S_{34}$  at threshold. The EFT error is estimated similarly to the  $^3{\rm He}(\alpha,\gamma)^7{\rm Be}$  reaction but now with  $Q\sim\gamma_0\sim 80$  MeV (and  $\Lambda\sim 200$  MeV). We included a 16% EFT error estimate from NNLO  $Q^2/\Lambda^2$  corrections. In this channel the binding energies are larger, resulting in a larger perturbation error compared to  $^3{\rm He}(\alpha,\gamma)^7{\rm Be}$ . Again, the actual theory error might be smaller for reasons similar to the  $^3{\rm He}(\alpha,\gamma)^7{\rm Be}$  reaction discussed earlier, and a more systematic estimate within the Bayesian framework [28–30] is left for the future.

The fits, especially without the phase shift data, give a central s-wave shape parameter value  $s_0$  that is larger than ideally expected from the power counting. Power counting consistency would bias one towards Model A (with phase shift) over Model A\* (without phase shift).

The EFT S-factor calculation can be compared to recent theoretical results – 0.12 keV b from FMD [31], 0.13 keV b from NCSM [32]; and experimental evaluation –  $[0.1067 \pm 0.0004(\mathrm{stat.}) \pm 0.0060(\mathrm{sys.})]$  keV b from Caltech [14].

Fit	$R_0$
$\chi^2$	$0.434 \pm 0.006 \pm 0.069$
Model A	$0.438^{+0.008}_{-0.009} \pm 0.070$
Model A*	$0.439^{+0.008}_{-0.009} \pm 0.070$

TABLE IV.  $^3\text{H}(\alpha, \gamma)^7\text{Li}$ : Branching ratio  $R_0$  at threshold (defined as  $E_{\star} = 60 \times 10^{-3}$  keV). The second set of errors are estimated from the EFT perturbation as detailed in the text.

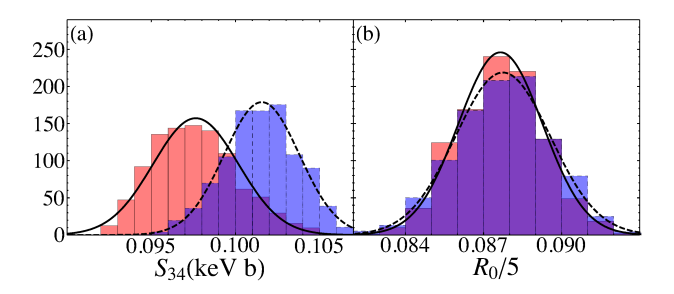


FIG. 8.  $^3\mathrm{H}(\alpha,\gamma)^7\mathrm{Li}$ : S-factor  $S_{34}$  and branching ratio  $R_0$  at threshold ( $E_\star=60\times10^{-3}~\mathrm{keV}$ ). The posterior distributions for fits Model A and Model A\* are presented as red and blue colored histograms, respectively. The corresponding Gaussian probability distributions are given by the solid and dashed curves, respectively.

We leave for future a more careful study of the systematic errors associated with the estimation of the parameters and evidences using the various NS methods. In our evaluations, for example, the MultiNest [21] and Diffusive Nested Sampling [34] algorithms gave similar

results. The EFT parameters (tables V and VI) agreed within the error bars. Similarly, the capture cross sections and branching ratios (tables I, II, III, IV) also agreed within the error bars from the fits.

References [35] and [36] were brought to our attention during the publication. These work consider finite-range corrections in s wave [35, 36] and p waves [35] using a short-ranged delta shell potential in Ref. [35] and zero-ranged square-well potential in Ref. [36], respectively. They find that in general effective range corrections are leading order effects in shallow systems in the strong Coulomb regime.

#### ACKNOWLEDGMENTS

The authors thank Barry Davids, Renato Higa, Daniel R. Phillips, Prakash Patil and Xilin Zhang for many valuable discussions. This work was supported in part by U.S. NSF grants PHY-1615092 and PHY-1913620. The figures for this article have been created using SciDraw [37].

### Appendix A: s and d wave capture

The capture from initial s-wave state is given by:

$$\frac{|\mathcal{A}(p)|}{C_0(\eta_p)} = \left| X(p) - \frac{2\pi}{\mu^2} \frac{B(p) + \mu J_0(p) + \mu^2 k_0 L_{E1}^{(\zeta)}}{[C_0(\eta_p)]^2 p(\cot \delta_0 - i)} \right|,$$
(A1)

where  $k_0$  is the photon energy and  $L_{E1}^{(\zeta)}$  for  $\zeta = {}^2P_{3/2}$  and  $\zeta = {}^2P_{1/2}$  are the 2 two-body currents. We modified some definitions compared to Ref. [2] but they are equivalent expressions.

The contribution without initial state strong interaction is given by

$$X(p) = 1 + \frac{2\gamma}{3} \frac{\Gamma(2 + k_C/\gamma)}{C_0(\eta_p)} \times \int_0^\infty dr \ rW_{-\frac{k_C}{\gamma}, \frac{3}{2}}(2\gamma r)\partial_r \left[\frac{F_0(\eta_p)}{pr}\right], \quad (A2)$$

where  $\gamma$  is the binding momentum of the ground or first excited state as appropriate. The momentum  $k_C = \alpha_e Z_\psi Z_\phi \mu$  is the inverse of the Bohr radius. The Coulomb expressions are:

$$F_{l}(\eta_{p}, \rho) = C_{l}(\eta_{p}) 2^{-l-1} (-i)^{l+1} M_{i\eta_{p}, l+1/2}(2i\rho) ,$$

$$C_{l}(\eta_{p}) = \frac{2^{l} e^{-\pi \eta_{p}/2} |\Gamma(l+1+i\eta_{p})|}{\Gamma(2l+2)} ,$$
(A3)

with conventionally defined Whittaker functions  $M_{k,\mu}(z)$  and  $W_{k,\mu}(z)$ .  $F_l(\eta_p,\rho)$  is the regular Coulomb wave function.

The initial s-wave scattering in Eq. (A1) is contained in the Coulomb subtracted phase shift  $\delta_0$  parameterized by the modified effective range expansion

$$[C_0(\eta_p)]^2 p(\cot \delta_0 - i) = -\frac{1}{a_0} + \frac{r_0}{2} p^2 + \frac{s_0}{4} p^4 + \cdots$$
$$-2k_C H(\eta_p),$$
$$H(x) = \psi(ix) + \frac{1}{2ix} - \ln(ix).$$
(A4)

 $\psi(x)$  is the digamma function, and the  $\cdots$  represents terms with higher powers in  $p^2$ . The combination  $B(p) + \mu J_0(p)$  can be evaluated as

$$B(p) + \mu J_0(p) = \frac{\mu^2}{3\pi} \frac{ip^3 - \gamma^3}{p^2 + \gamma^2} + k_C C(p) + \Delta B(p)$$
$$-\frac{k_C \mu^2}{2\pi} \left[ 2H(\eta_p) + 2\gamma_E - \frac{5}{3} + \ln 4\pi \right] . \quad (A5)$$

The function C(p) is given by the double integral

$$C(p) = \frac{\mu^2}{6\pi^2(p^2 + \gamma^2)} \int_0^1 dx \int_0^1 dy \frac{1}{\sqrt{x(1-x)}\sqrt{1-y}} \times \left( xp^2 \ln \left[ \frac{\pi}{4k_C^2} (-yp^2 + (1-y)\gamma^2/x - i\delta) \right] + p^2 \ln \left[ \frac{\pi}{4k_C^2} (-yp^2 - (1-y)p^2/x - i\delta) \right] + x\gamma^2 \ln \left[ \frac{\pi}{4k_C^2} (y\gamma^2 + (1-y)\gamma^2/x - i\delta) \right] + \gamma^2 \ln \left[ \frac{\pi}{4k_C^2} (y\gamma^2 - (1-y)p^2/x - i\delta) \right] \right), \quad (A6)$$

which is reduced to a single integral before evaluating numerically. The function  $\Delta B(p)$  is obtained from

$$B_{ab}(p) = -3 \int d^3r \left[ \frac{G_C^{(1)}(-B; r', r)}{r'} \right] \Big|_{r'=0}$$

$$\times \frac{\partial G_C^{(+)}(E; \mathbf{r}, 0)}{\partial r_a} \frac{r_b}{r} ,$$

$$\left[ \frac{G_C^{(1)}(-B; r', r)}{r'} \right] \Big|_{r'=0} = -\frac{\mu \gamma}{6\pi r} \Gamma(2 + k_C/\gamma) W_{-\frac{k_C}{\gamma}, \frac{3}{2}}(2\gamma r) ,$$

$$G_C^{(+)}(E; \mathbf{r}, 0) = -\frac{\mu}{2\pi r} \Gamma(1 + i\eta_p) W_{-i\eta_p, \frac{1}{2}}(-i2pr) . \quad (A7)$$

The integral  $B_{ab}(p)$  is divergent at r=0. However, when combined with the contribution from  $J(p)\delta_{ab}$  it is finite. Thus we make the substitution  $(r_b/r)[\partial/\partial r_a] = (r_a r_b/r^2)[\partial/\partial r] \to (\delta_{ab}/3)[\partial/\partial r]$  in the integral and accordingly  $B_{ab}(p) \equiv B(p)\delta_{ab}$ . The finite piece  $\Delta B(p)$  is obtained numerically from B(p) after subtracting the zero and single photon contributions i.e. removing terms up to order  $\alpha_e^2$  [2].

The capture from initial d-wave states is given by the amplitude [2]:

$$Y(p) = \frac{2\gamma}{3}\Gamma(2 + k_C/\gamma) \int_0^\infty dr \ r W_{-k_C/\gamma, 3/2}(2\gamma r) \times \left(\frac{\partial}{\partial r} + \frac{3}{r}\right) \frac{F_2(\eta_p, rp)}{rp} . \quad (A8)$$

#### Appendix B: Wave function renormalization

The wave function renormalization constant is calculated as [2]:

$$-\frac{2\pi}{h^{(\zeta)2}\mathcal{Z}^{(\zeta)}} = \frac{1}{p} \frac{\partial}{\partial p} 9[C_1(\eta_p)]^2 p^3(\cot \delta_1 - i)$$

$$= \rho_1^{(\zeta)} - 4k_C H \left(-i\frac{k_C}{\gamma}\right) - \frac{2k_C^2}{\gamma^3} (k_C^2 - \gamma^2)$$

$$\left[\psi'\left(\frac{k_C}{\gamma}\right) - \frac{\gamma^2}{2k_C^2} - \frac{\gamma}{k_C}\right], \quad (B1)$$

where we used the relation

$$9[C_1(\eta_p)]^2 p^3(\cot \delta_1 - i) = 2k_C (k_C^2 - \gamma^2) H(-i\eta_\gamma)$$

$$+ \frac{1}{2} \rho_1 (p^2 + \gamma^2) + \frac{1}{4} \sigma_1 (p^2 + \gamma^2)^2 + \cdots$$

$$- 2k_C (k_C^2 + p^2) H(\eta_p). \quad (B2)$$

## **Appendix C: Parameter Estimates**

We list the parameter estimates for both  ${}^3{\rm He}(\alpha,\gamma){}^7{\rm Be}$  and  ${}^3{\rm H}(\alpha,\gamma){}^7{\rm Li}$  in tables V and VI, respectively. For the Bayesian fits we show the median and the bounds containing 68% of the posterior distributions. Typically, a very asymmetric bound indicates either a skewed or sometimes a bi-modal distribution.

### **Appendix D: Parameter Correlations**

We include the so called corner plots [38] in Figs 9, 10, 11, 12, 13, 14, and 15 for the parameters from the MultiNest algorithm [21] implemented in Python [22]. The plots show around 99% of the posterior distribution around the median. We include only those fits where the estimated parameter values were consistent with the EFT power counting expectations. We set the precision in the logarithm of the evidences to 0.3. The default suggested precision is 0.5. MultiNest is an adaptive algorithm that adjusts the MCMC calls based on the desired precision. Usually, twice as many "live" points as parameters is suggested in fits [22]. We used 100-120 live points in the fits which was adequate given our fits with atmost 10 parameters. We tested the numerical stability by using a range 40-120 of live points  $n_{\rm live}$  in MultiNest. We compared the

Fits	$a_0 \text{ (fm)}$	$r_0$ (fm)	$s_0 \; (\mathrm{fm}^3)$	$\rho_1^{(+)} \; (\mathrm{MeV})$	$\sigma_1^{(+)}$ (fm)	$\rho_1^{(-)} \; (\mathrm{MeV})$	$\sigma_1^{(-)}$ (fm)	$L_1^{(+)}$	$L_1^{(-)}$	K
$\chi^2$	$22 \pm 3$	$1.2 \pm 0.1$	$-0.89\pm0.7$	$-55.4 \pm 0.5$	$1.59 \pm 0.03$	$-41.9 \pm 0.7$	$1.74 \pm 0.05$	$0.78 \pm 0.06$	$0.83 \pm 0.08$	_
Model A I	$48^{+2}_{-2}$	$1^{+0.08}_{-0.1}$	$-1.8^{+0.9}_{-0.8}$	$-72^{+5}_{-7}$	$2.1^{+0.2}_{-0.2}$	$-49^{+3}_{-5}$	$2^{+0.2}_{-0.1}$	$1.4^{+0.2}_{-0.1}$	$1.2^{+0.2}_{-0.1}$	$0.3^{+0.3}_{-0.2}$
Model B I	$38^{+2}_{-2}$	$1.1^{+0.1}_{-0.1}$	$-2^{+0.9}_{-1}$	$-61.6^{+0.5}_{-0.5}$	$1.77^{+0.03}_{-0.03}$	$-48^{+1}_{-6}$	$2^{+0.2}_{-0.07}$	$1.13^{+0.03}_{-0.02}$	$1.2^{+0.2}_{-0.07}$	$0.3^{+0.3}_{-0.2}$
Model A* I	$20^{+7}_{-5}$	$-0.1^{+0.5}_{-0.6}$	$-16^{+6}_{-7}$	$-89^{+9}_{-10}$	_	$-130^{+40}_{-60}$	_	$3^{+1}_{-0.8}$	$7^{+2}_{-3}$	_
Model B* I	$37^{+3}_{-8}$	$1.1^{+0.1}_{-0.7}$	_	$-61.4^{+1}_{-0.7}$	_	$-47^{+2}_{-4}$	_	$1.14^{+0.08}_{-0.04}$	$1.2^{+0.2}_{-0.1}$	_
Model A II	$40^{+5}_{-6}$	$1.09^{+0.09}_{-0.1}$	$-2.2^{+0.7}_{-0.7}$	$-59^{+1}_{-1}$	$1.69^{+0.05}_{-0.05}$	$-45^{+1}_{-2}$	$1.84^{+0.07}_{-0.07}$	$1.02^{+0.05}_{-0.05}$	$1.07^{+0.07}_{-0.08}$	$0.3^{+0.3}_{-0.2}$
Model B II	$7.3^{+0.6}_{-0.7}$	$1.31^{+0.02}_{-0.02}$	$6^{+1}_{-1}$	$-53.5^{+0.1}_{-0.1}$	$1.53^{+0.05}_{-0.05}$	$-40.1^{+0.2}_{-0.2}$	$1.67^{+0.06}_{-0.06}$	$-0.04^{+0.08}_{-0.1}$	$-0.01^{+0.08}_{-0.1}$	$2.2^{+0.6}_{-0.4}$
Model A* II	$46^{+10}_{-3}$	$1^{+0.1}_{-0.3}$	$-3^{+5}_{-2}$	$-62^{+4}_{-3}$	_	$-51^{+4}_{-60}$	_	$1.1^{+0.1}_{-0.1}$	$1.3^{+1}_{-0.1}$	_
Model B* II	$5^{+0.9}_{-2}$	$1.24^{+0.04}_{-0.1}$	_	$-53.5^{+0.1}_{-0.1}$	_	$-40.2^{+0.2}_{-0.2}$	_	$-0.5^{+0.2}_{-0.8}$	$-0.4^{+0.2}_{-0.8}$	_

TABLE V.  $^3\text{He}(\alpha, \gamma)^7\text{Be}$ : EFT parameters. We estimate the parameters from fits to capture data in region I  $(E \lesssim 1000 \text{ keV})$  and in region II  $(E \lesssim 2000 \text{ keV})$  as indicated. The fits that do not use elastic scattering phase shift data are indicated by the asterisk \* sign. We show the errors to one significant figure.

Fits	$a_0$ (fm)	$r_0$ (fm)	$s_0 \text{ (fm}^3\text{)}$	$\rho_1^{(+)} \; ({\rm MeV})$	$\rho_1^{(-)} \; (\mathrm{MeV})$	$L_1^{(+)}$	$L_1^{(-)}$	K
$\chi^2$	$17 \pm 2$	$0.6 \pm 0.3$	$2\pm 2$	$-149 \pm 3$	$-129 \pm 4$	$1.44 \pm 0.07$	$1.5 \pm 0.1$	-
Model A	$13^{+1}_{-1}$	$0^{+0.5}_{-0.7}$	$11^{+9}_{-7}$	$-190^{+30}_{-30}$	$-230^{+70}_{-60}$	$2.2^{+0.6}_{-0.6}$	$4^{+1}_{-2}$	$2^{+2}_{-1}$
Model B	$21^{+2}_{-2}$	$2.7^{+0.09}_{-0.09}$	$-24^{+2}_{-2}$	$-219^{+8}_{-8}$	$-200^{+10}_{-9}$	$2.14^{+0.01}_{-0.01}$	$2.4^{+0.1}_{-0.1}$	$6^{+2}_{-1}$
Model A*	$10^{+2}_{-2}$	$-2^{+0.7}_{-0.8}$	$36^{+6}_{-8}$	$-220^{+30}_{-30}$	$-240^{+40}_{-50}$	$3.3^{+0.8}_{-0.8}$	$5^{+1}_{-1}$	_
Model B*	$20^{+1}_{-1}$	$2.7^{+0.09}_{-0.09}$	-	$-213^{+5}_{-4}$	$-191^{+7}_{-6}$	$2.14^{+0.01}_{-0.01}$	$2.37^{+0.09}_{-0.08}$	_

TABLE VI.  $^{3}$ H $(\alpha, \gamma)^{7}$ Li: EFT parameters. The fits that do not use elastic scattering phase shift data are indicated by the asterisk \* sign. We show the errors to one significant figure.

results from MuliNest with fits from the original Nested Sampling algorithm [20] implemented with our own Fortran code. We tested with few hundred live points  $n_{\rm live}$ , using about  $10^5$  MCMC steps per sample point for a sample size of about  $100 \times n_{\rm live}$  (total  $10^7 \times n_{\rm live}$  MCMC calls). The original NS algorithm is not as efficient as the adaptive algorithms as pointed out in literature such as Refs. [21, 34] though it provides an independent verification where we can control the parameters of MCMC simulations more directly.

#### Appendix E: Accuracy and Precision

The EFT power counting comparisons performed in this work is different than the typical Bayesian model comparisons where two or more models with fixed but possibly different number of parameters are compared. In the literature, EFT calculations are considered modelindependent though we call the two power countings Model A and Model B in accordance to the practice in the field of Bayesian analysis. In the construction of an EFT, once the low-energy degrees of freedom and the low-energy symmetries are identified, no attempt is made in modeling the high-energy physics. The relevant halo EFT symmetries do not preclude considering terms in the Lagrangian with mass dimensions greater than 4. As a consequence, the EFTs are non-renormalizable field theories that contain infinitely many terms (and unknown couplings) in principle. However, in practice an expansion in a small parameter  $Q/\Lambda$  where Q is a typical small momentum and  $\Lambda$  some higher momentum scale is constructed. Then usually only a finite number of terms (and unknown couplings) from the Lagrangian is relevant at a given order of the expansion.

The LO contributions in Model A and Model B differ. They contain different Feynman diagrams. Thus these two theories reproduce the true value with different accuracies at LO. Higher order contributions should bring them closer to the true value (assuming they have consistent convergence properties). However, the estimate  $Q/\Lambda$  from NLO contributions, for example, is too naïve. This is just a conservative estimate that does not capture the functional dependence on  $p/\Lambda$  and  $p/\gamma$  correctly, where p is the incoming momentum and  $\gamma$  is the binding momentum. The following example demonstrates some of these ideas.

Suppose we consider the s-wave scattering of two neutral particles of mass m at low momentum  $p \ll 1/R$  where R is the range of the two-particle interaction. The exact analytic form of the T-matrix is known [39–41], which is given by the effective range expansion as:

$$T(p) = \frac{4\pi}{m} \frac{1}{-\frac{1}{a_0} + \frac{1}{2}r_0p^2 + \frac{1}{4}s_0p^4 + \dots - ip}.$$
 (E1)

We can imagine a system where say 1/R = 200 MeV,  $1/a_0 = -10$  MeV,  $1/r_0 = 30$  MeV, and the rest of the scattering parameters are of natural size given by appropriate powers of R such as  $s_0 = R^3$ , etc. Associating  $p \lesssim 70$  MeV with the low momentum scale Q, we can

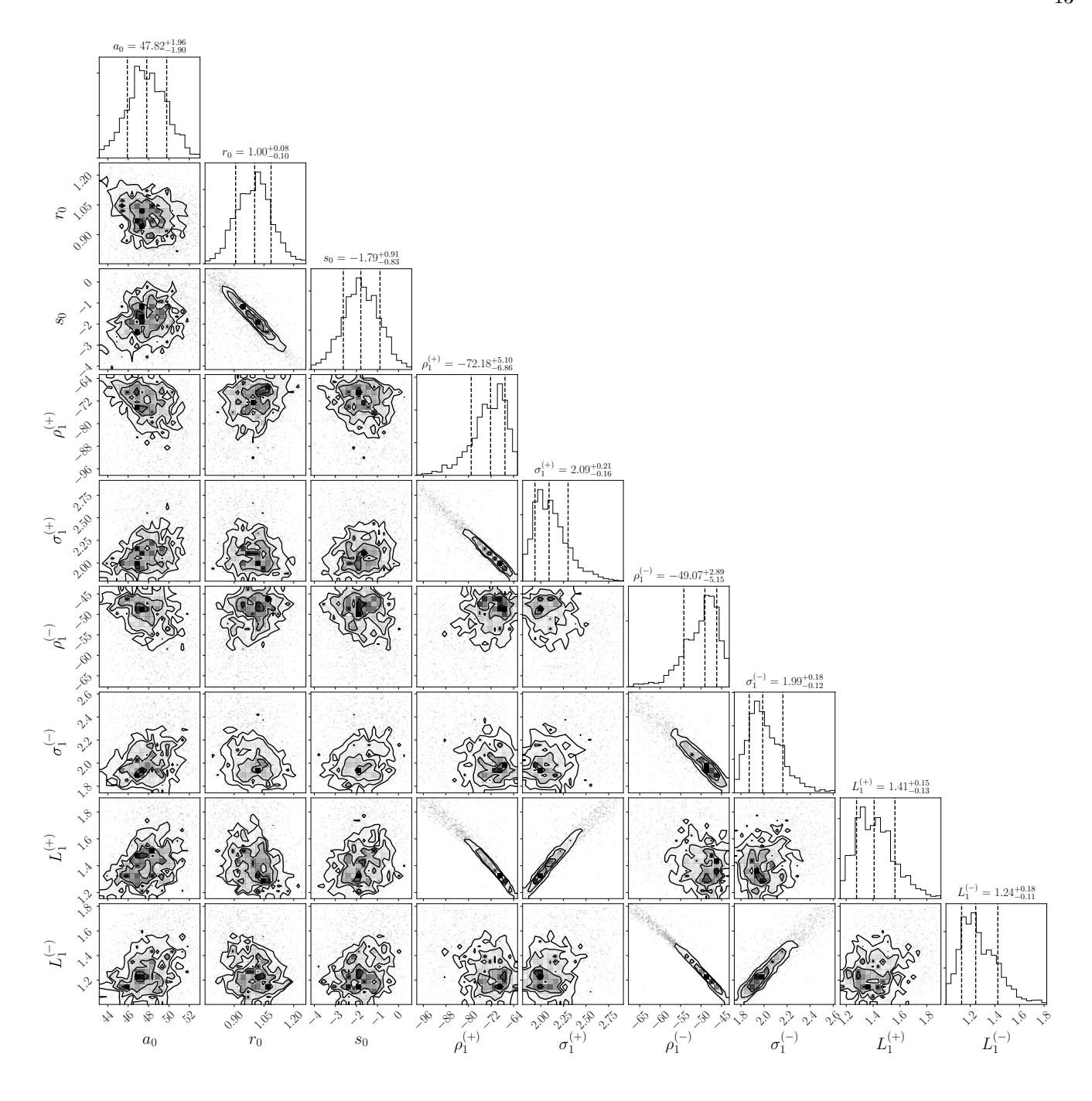


FIG. 9.  ${}^{3}\text{He}(\alpha,\gamma){}^{7}\text{Be}$ : The posteriors for the parameters  $a_0$  in fm,  $r_0$  in fm,  $s_0$  in fm<sup>3</sup>,  $\rho_1^{(+)}$  in MeV,  $\sigma_1^{(+)}$  in fm,  $\rho_1^{(-)}$  in fm  $\rho_1^{(-)}$  in fm and  $L_1^{(\pm)}$ , respectively, in Model A I from 5220 samples. Parameter K (not shown) didn't show strong correlation with the others. The vertical dashed lines indicate the median and the interval containing 68% of the posterior distribution around the median, table V.

use the usual pionless EFT expansion [42, 43] and construct a power counting (Model 1) where  $1/|a| \sim Q$  and the rest of the scattering parameters including  $r_0$  scales with appropriate powers of R. However, the size of the effective range  $r_0$  is intermediate between  $Q \sim 1/|a|$  and 1/R, and it is a priori not clear how one should classify it. Thus, one can construct an alternate power counting

(Model 2) with  $1/r_0 \sim Q$ . As the reader might notice, these  $a_0$ ,  $r_0$  values are not physically irrelevant as they are close to the ones for neutron-proton scattering in the  ${}^1S_0$  channel where  $a_0 \approx -8.31$  MeV,  $r_0 \approx 72.3$  MeV. The

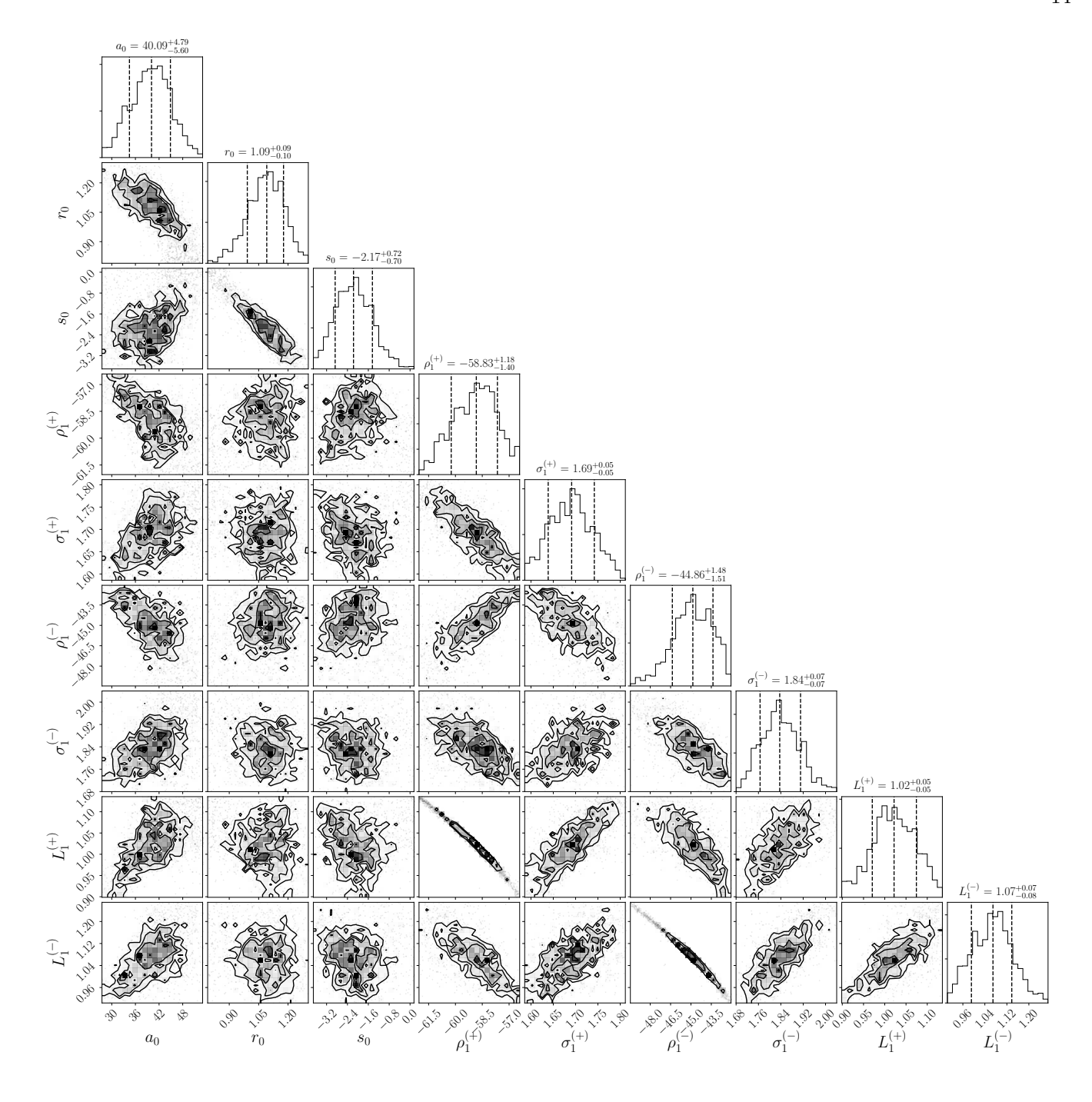


FIG. 10.  ${}^{3}\text{He}(\alpha,\gamma){}^{7}\text{Be}$ : The posteriors for the parameters  $a_0$  in fm,  $r_0$  in fm,  $s_0$  in fm<sup>3</sup>,  $\rho_1^{(+)}$  in MeV,  $\sigma_1^{(+)}$  in fm,  $\rho_1^{(-)}$  in MeV,  $\sigma_1^{(-)}$  in fm and  $L_1^{(\pm)}$ , respectively, in Model A II from 5816 samples. Parameter K (not shown) didn't show strong correlation with the others. The vertical dashed lines indicate the median and the interval containing 68% of the posterior distribution around the median, table V.

two theories expanded to NLO gives

for Model 1, and

$$T^{(1)}(p) = -\frac{4\pi}{m} \frac{1}{\frac{1}{a_0} + ip} \left[ 1 + \frac{r_0 p^2 / 2}{\frac{1}{a_0} + ip} \right] , \qquad (E2)$$

$$T^{(2)}(p) = -\frac{4\pi}{m} \frac{1}{\frac{1}{a_0} - \frac{1}{2}r_0p^2 + ip} \left[ 1 + \frac{s_0p^4/4}{\frac{1}{a_0} - \frac{1}{2}r_0p^2 + ip} \right],$$
(E3)

for Model 2. The amplitudes  $T^{(1)}$  and  $T^{(2)}$  both scale

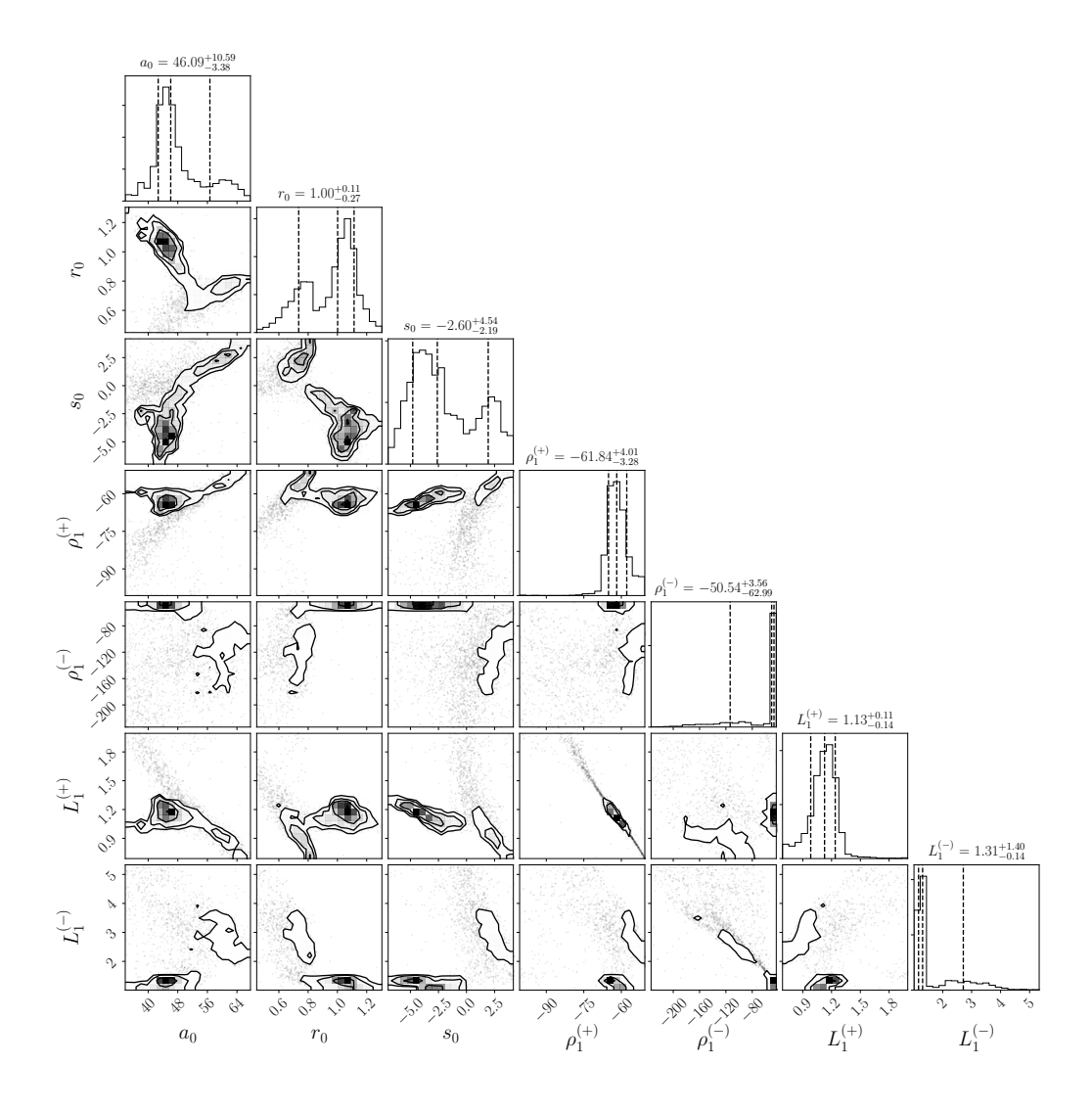


FIG. 11.  ${}^{3}\text{He}(\alpha, \gamma)^{7}\text{Be}$ : The posteriors for the parameters  $a_0$  in fm,  $r_0$  in fm,  $s_0$  in fm<sup>3</sup>,  $\rho_1^{(\pm)}$  in MeV and  $L_1^{(\pm)}$ , respectively, in Model A\* II from 4100 samples. The vertical dashed lines indicate the median and the interval containing 68% of the posterior distribution around the median, table V.

as 1/Q at LO but they differ at non-zero momentum p. The NLO contribution in Model 1 is of relative  $\mathcal{O}(Q/\Lambda)$  whereas in Model 2 it is  $\mathcal{O}(Q^3/\Lambda^3)$ . Moreover, the functional dependence on p is also different at NLO.

The radiative capture reactions  ${}^3{\rm He}(\alpha,\gamma){}^7{\rm Be}$  and  ${}^3{\rm H}(\alpha,\gamma){}^7{\rm Li}$  at low momentum do not have a simple expansion in p, like the example above, due to the Coulomb interaction. However, the general principle still holds. Comparing the theories at the same order of the  $Q/\Lambda$  expansion would not achieve the same level of accuracy since the LO contributions are different. It will also not necessarily achieve the same level of precision because the conservative estimate  $Q/\Lambda$  of error from higher order corrections is too naïve. It does not capture the momentum p dependence precisely.

We want to address the question: Given two EFTs with different accuracies and precisions, how does one perform a Bayesian "model" comparisons? One can make

different decisions. We compare them at the same level of accuracy which seems physically reasonable as we explain next.

EFTs with unknown couplings are undefined. Imposing renormalization conditions (matching conditions) fixes the couplings and defines the theory though in practice EFT couplings are often determined by fitting cross sections over a range of momentum. However, one still theoretically associates the couplings with renormalization conditions. Ref. [44] demonstrates this in chiral perturbation theory ( $\chi$ PT) up to NNLO for nucleon-nucleon scattering where 6 couplings are determined from matching conditions. In the  $\chi$ PT calculations, the matching conditions could be imposed analytically. It is equivalent to requiring the EFT calculation to reproduce the scattering amplitude at 6 "training data" points exactly. In this case at 6 low momenta in an arbitrarily small neighborhood around the virtual pole in the  $^1S_0$  T-matrix [44].

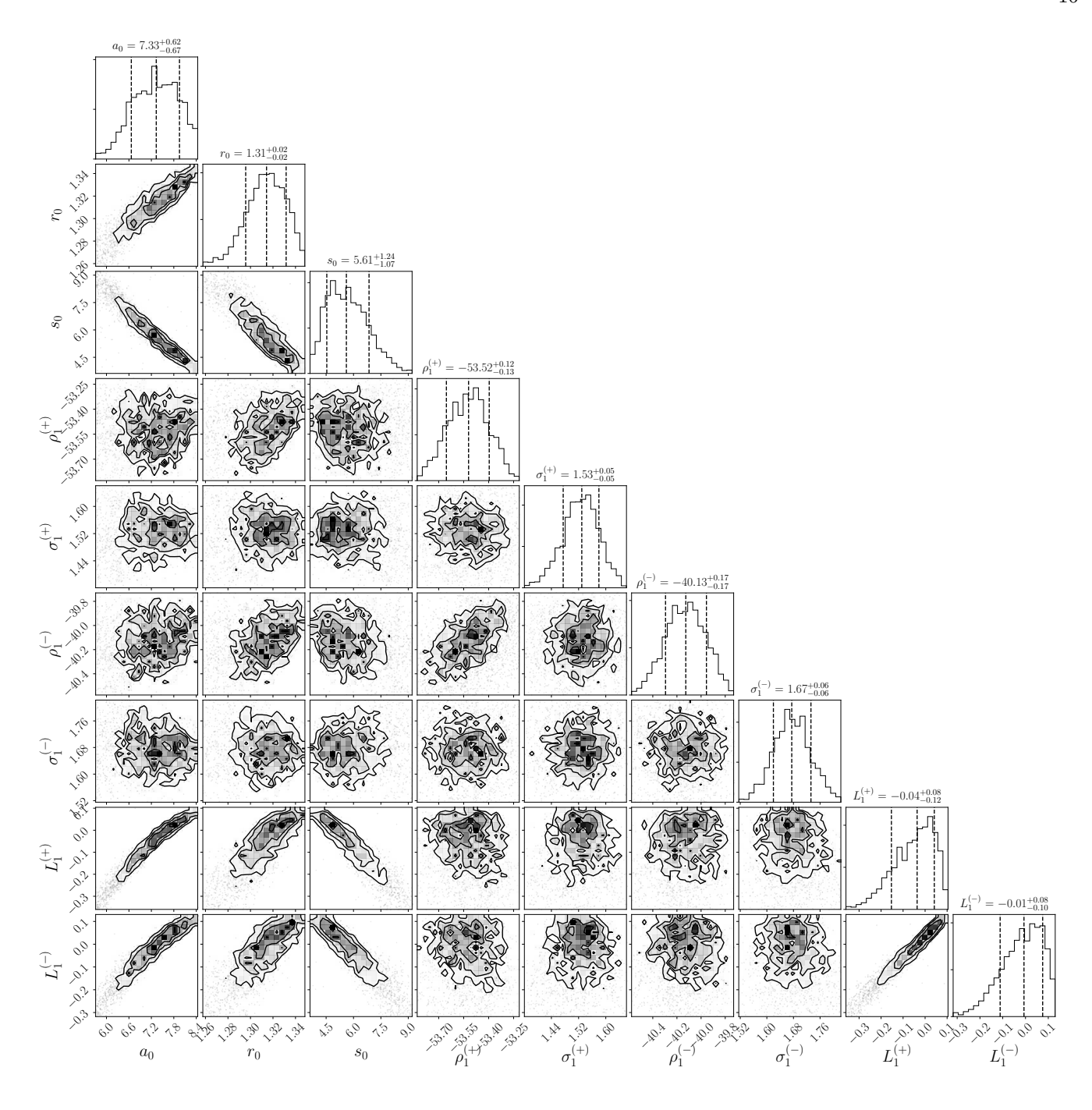


FIG. 12.  ${}^{3}\text{He}(\alpha,\gamma){}^{7}\text{Be}$ : The posteriors for the parameters  $a_0$  in fm,  $r_0$  in fm,  $s_0$  in fm<sup>3</sup>,  $\rho_1^{(+)}$  in MeV,  $\sigma_1^{(+)}$  in fm,  $\rho_1^{(-)}$  in MeV,  $\sigma_1^{(-)}$  in fm and  $L_1^{(\pm)}$ , respectively, in Model B II from 5895 samples. Parameter K (not shown) didn't show strong correlation with the others. The vertical dashed lines indicate the median and the interval containing 68% of the posterior distribution around the median, table V.

The EFT calculation is then validated by predicting the phase shift and comparing with data over a range of momenta [44]. The lecture notes in Ref. [45] has further examples from particle physics on matching conditions in EFTs.

Unlike in the  $\chi$ PT nucleon-nucleon scattering calculation [44], in the capture reaction we do not know the

analytic form of the exact capture cross section. We can only insist that the EFTs reproduce cross sections at certain low-momenta data points exactly to define the couplings and the theories. In essence we achieve the same accuracy in the two power countings by imposing the same matching conditions i.e. the EFTs reproduce the same set of training data points exactly. In par-

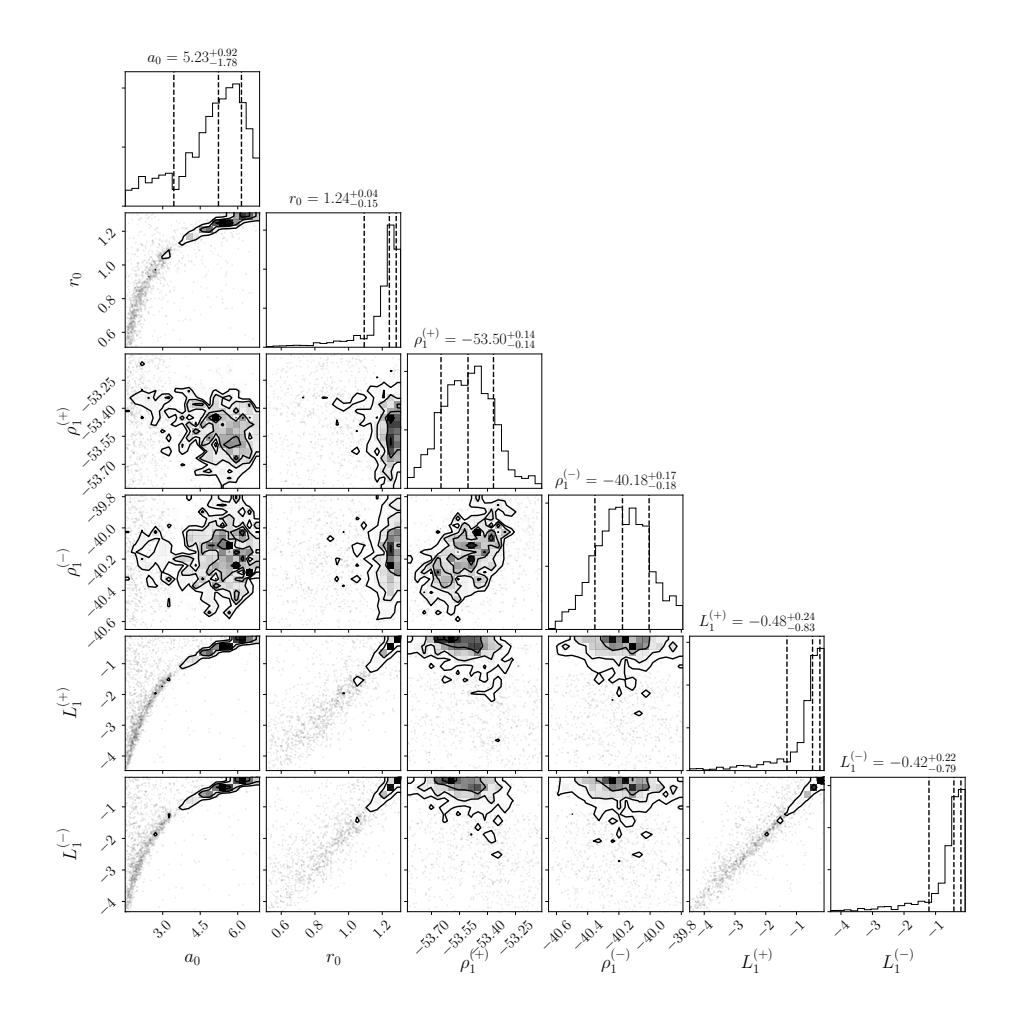


FIG. 13.  ${}^{3}\text{He}(\alpha, \gamma){}^{7}\text{Be}$ : The posteriors for the parameters  $a_0$  in fm,  $r_0$  in fm,  $\rho_1^{(\pm)}$  in MeV and  $L_1^{(\pm)}$ , respectively, in Model B\* II from 4573 samples. The vertical dashed lines indicate the median and the interval containing 68% of the posterior distribution around the median, table V.

ticular both the EFTs reproduce the s-wave scattering length  $a_0$ , effective range  $r_0$ , and shape parameter  $s_0$ exactly, which physically means we are imposing renormalization conditions on the elastic scattering amplitude and its derivatives at zero momentum. Reproducing the p-wave binding momentum  $\gamma$  and effective range  $\rho_1$  is a renormalization condition on the location of the pole and the residue of the T-matrix. The two-body currents are renormalization conditions to reproduce the charge radii of the ground and excited final states. Then the EFTs are validated by checking how well they reproduce the data at the higher momenta. Experimentally we only know the charge radii of the ground states of <sup>7</sup>Be and <sup>7</sup>Li. However, this is not an issue in practice since we fit the couplings to the capture cross sections over a momentum range. Alternatively, we can predict the charge radii of the excited states from the fitted two-body currents. An

important requirement in deciding on the minimum number of matching conditions is that one should determine all the couplings at a given order in the expansion. For example, imposing 3 matching conditions in "Model A" would constrain 3 LO couplings but leave 3 other LO couplings undetermined. This is inconsistent. Working in an iterative manner, one can see that imposing 6 matching conditions would determine all 6 LO couplings in Model A, and consistently determine all couplings in Model B up to NLO (when considering both capture and phase shift data). Similarly, 9 matching conditions determines all NLO couplings in Model A and all NNLO couplings in Model B capture (NLO in phase shift). Again, in practice, we determine the EFT couplings by fitting them to data over a momentum range, and then compare the two EFT power countings at the same level of accuracy.

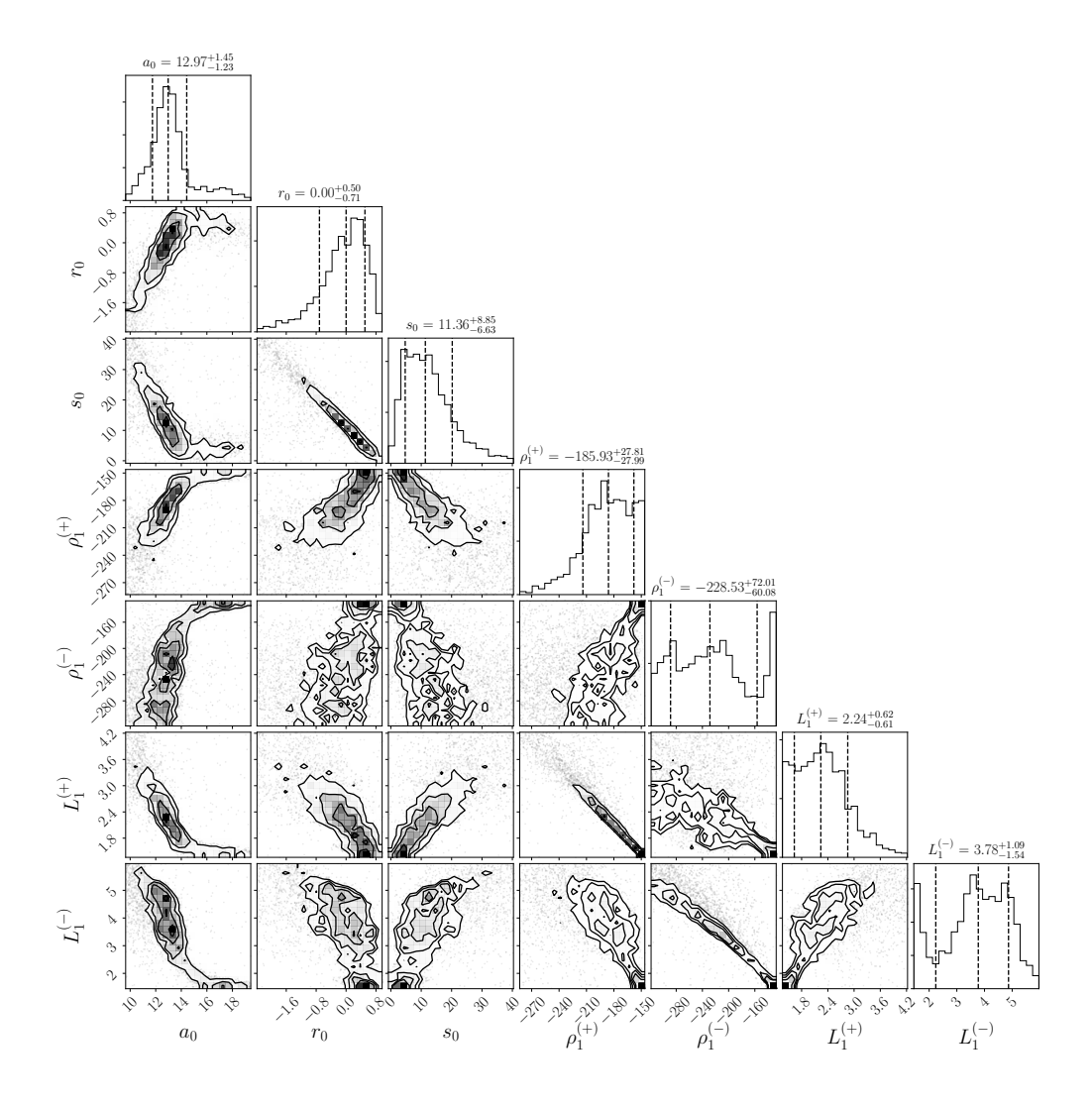


FIG. 14.  ${}^{3}\text{H}(\alpha, \gamma)^{7}\text{Li}$ : The posteriors for the parameters  $a_{0}$  in fm,  $r_{0}$  in fm,  $s_{0}$  in fm<sup>3</sup>,  $\rho_{1}^{(\pm)}$  in MeV and  $L_{1}^{(\pm)}$ , respectively, in Model A from 4153 samples. Parameter K (not shown) didn't show strong correlation with the others. The vertical dashed lines indicate the median and the interval containing 68% of the posterior distribution around the median, table VI.

- 89 (2018).
- [3] S. Fukuda *et al.* (Super-Kamiokande), Phys. Rev. Lett. 86, 5651 (2001).
- [4] B. Aharmin *et al.* (SNO), Phys. Rev. **C75**, 045502 (2007).
- [5] J. N. Bahcall and R. K. Ulrich, Rev. Mod. Phys. 60, 297 (1988).
- [6] R. Cyburt and B. Davids, Phys. Rev. C78, 064614 (2008).
- [7] A. Di Leva et al., Phys. Rev. Lett 102, 232502 (2009).
- [8] H. Constantini et al., Nucl. Phys. A 814, 144 (2008).
- [9] A. Kontos, E. Uberseder, R. deBoer, J. Görres, C. Akers, A. Best, M. Couder, and M. Wiescher, Phys. Rev. C87, 065804 (2013), [Addendum: Phys. Rev.C88,no.1,019906(2013)].
- [10] T. A. D. Brown et al., Phys. Rev. C 76, 055801 (2007).
- [11] B. S. Nara Singh, M. Hass, Y. Nir-El, and G. Haquin, Phys. Rev. Lett. 93, 262503 (2004).
- [12] L. H. Kawano, W. A. Fowler, R. W. Kavanagh, and R. A. Malaney, Astrophys. J. 372, 1 (1991).

- [13] M. S. Smith, L. H. Kawano, and R. A. Malaney, Astrophys. J., Suppl. Ser. 85, 219 (1993).
- [14] C. R. Brune, R. W. Kavanagh, and C. Rolfs, Phys. Rev. C 50, 2205 (1994).
- [15] V. M. Bystritsky et al., Phys. Part. Nucl. Lett. 14, 560 (2017).
- [16] C. A. Bertulani, H. W. Hammer, and U. Van Kolck, Nucl. Phys. A712, 37 (2002).
- [17] P. F. Bedaque, H. W. Hammer, and U. van Kolck, Phys. Lett. **B569**, 159 (2003).
- [18] G. Rupak, Int. J. Mod. Phys. **E25**, 1641004 (2016).
- [19] B. J. Brewer, in *Bayesian Astrophysics*, Canary Islands Winter School of Astrophysics, edited by A. Ramos and Í. Arregui (Cambridge University Press, 2018) pp. 1–30.
- [20] J. Skilling, Bayesian Analysis 1, 833 (2006).
- [21] F. Feroz, M. P. Hobson, and M. Bridges, Mon. Not. R. Astron. Soc. 398, 1601 (2009).
- [22] K. Barbary, "Nestle," https://github.com/kbarbary/
- [23] R. J. Spieger and T. A. Tombrello, Phys. Rev. 163, 964

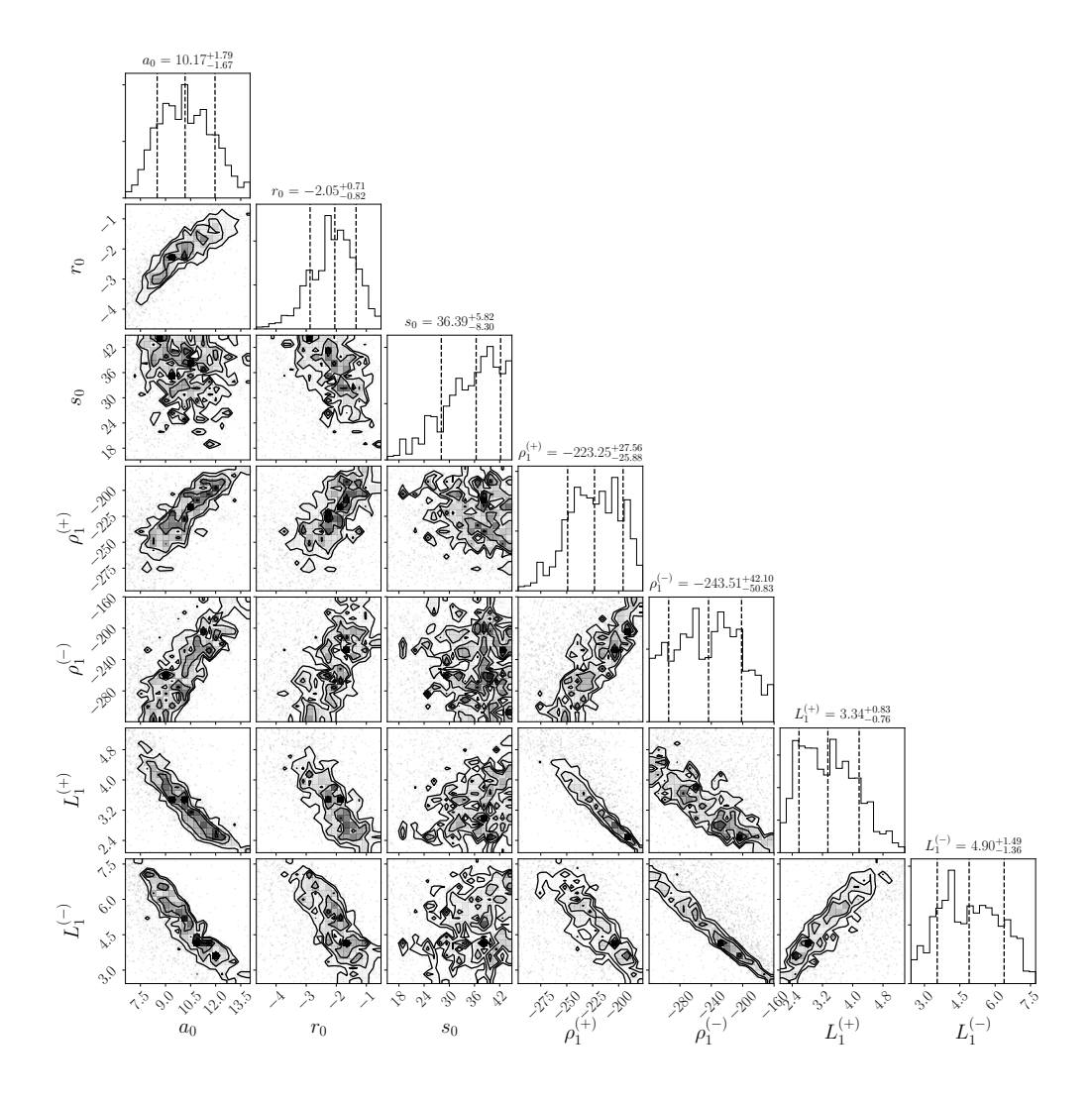


FIG. 15.  ${}^{3}\text{H}(\alpha, \gamma)^{7}\text{Li}$ : The posteriors for the parameters  $a_{0}$  in fm,  $r_{0}$  in fm,  $s_{0}$  in fm<sup>3</sup>,  $\rho_{1}^{(\pm)}$  in MeV and  $L_{1}^{(\pm)}$ , respectively, in Model A\* from 2916 samples. The vertical dashed lines indicate the median and the interval containing 68% of the posterior distribution around the median, table VI.

(1967).

- [24] W. R. Boykin, S. D. Baker, and D. M. Hardy, Nucl. Phys. A 195, 241 (1972).
- [25] R. Higa, H.-W. Hammer, and U. van Kolck, Nucl. Phys. A809, 171 (2008).
- [26] B. Davids, "Elastic scattering of  $^{3}\text{He}+\alpha$  with SONIK," (2016), private communication.
- [27] T. A. Tombrello and P. D. Parker, Phys. Rev. 131, 2582 (1963).
- [28] R. J. Furnstahl, D. R. Phillips, and S. Wesolowski, J. Phys. G42, 034028 (2015).
- [29] R. J. Furnstahl, N. Kleo, D. R. Phillips, and S. Wesolowski, Phys. Rev. C92, 024005 (2015).
- [30] J. A. Melendez, R. J. Furnstahl, D. R. Phillips, M. T. Pratola, and S. Wesolowski, (2019), arXiv:1904.10581 [nucl-th].
- [31] T. Neff, Phys. Rev. Lett. **106**, 042502 (2011).
- [32] J. Dohet-Eraly et al., Phys. Lett. B757, 430 (2016).
- [33] X. Zhang, K. M. Nollett, and D. R. Phillips (2018) arXiv:1811.07611 [nucl-th].

- [34] B. J. Brewer, L. B. Pártay, and G. Csányi, Statistics and Computing 21, 649 (2011).
- [35] B. K. Luna and T. Papenbrock, Phys. Rev. C100, 054307 (2019).
- [36] C. H. Schmickler, H. W. Hammer, and A. G. Volosniev, Phys. Lett. B798, 135016 (2019).
- [37] M. A. Caprio, Comput. Phys. Commun. 171, 107 (2005), http://scidraw.nd.edu.
- [38] D. Foreman-Mackey, The Journal of Open Source Software 24 (2016), 10.21105/joss.00024.
- [39] J. Schwinger, Harvard lecture notes. Quoted by J. Blatt in Phys. Rev. 74, 92 (1948).
- [40] H. A. Bethe, Phys. Rev. **76**, 38 (1949).
- [41] H. W. Hammer and D. Lee, Annals Phys. 325, 2212 (2010).
- [42] P. F. Bedaque and U. van Kolck, Phys. Lett. B428, 221 (1998).
- [43] J.-W. Chen, G. Rupak, and M. J. Savage, Nucl. Phys. A653, 386 (1999).
- [44] G. Rupak and N. Shoresh, Phys. Rev. C60, 054004

(1999).

[45] A. V. Manohar, Perturbative and nonperturbative aspects of quantum field theory. Proceedings, 35. Internationale Universitätswochen für Kern- und Teilchen-

physik: Schladming, Austria, March 2-9, 1996, Lect. Notes Phys. 479, 311 (1997), arXiv:hep-ph/9606222 [hep-ph].